CARE WORKSHOP

EurAAP

CORE

SEVENTH FRAMEWORK PROGRAMME

FP7 COORDINATION ACTION "CARE"
FINAL WORKSHOP

Organized in conjunction with EuCAP 2012.
Prague Congress Centre, Prague, Czech Republic,
28 March 2012, 14:00–16:40 , Room Club A

14h00-14h15 Welcome and CARE project overview
Bruno Casali, CARE Coordinator, IDS Italy

14h15-14h30 CARE project factsheet: WGs, results and achieved impact.
Bruno Casali, CARE Coordinator, IDS Italy

SECONDMENTS PRESENTATIONS

14h30-14h45
High Resolution Two-Dimensional DOA Estimation Using Artificial Neural Networks
Marija Agatonovic (1), Zoran Stankovic (1), Bratislav Milovanovic (1), Y. Leen Sit (2) and Thomas Zwick (2)
(1) Faculty of Electronic Engineering, University of Nis, Serbia
(2) Karlsruhe Institute of Technology, Germany

14h45-15h00
Design and Analysis of a Planar UHF Wearable Antenna
Branimir Ivsic (1), Juraj Bartolic (1), Davor Bonefacic (1), Anja K Skrivervik (2), Jovanche Trajkovikj (2)
(1) University of Zagreb, Croatia
(2) EPFL, Switzerland

15h00-15h15
Evaluation of Specific Absorption Rate and radiation pattern features for a dozen of wearable antennas operating from 600 MHz to 5.5 GHz
Tomasz Maleszka (1), Witold Kurp (1), Andre van den Bosch (2), Steffan Weitz (2), Marta Martinez (2)
(1)Wroclaw University of Technology, Wroclaw, Poland
(2) IMST, Kamp Lintfort, Germany

15h15-15h30
RHCP patch antenna element for Telecommand, Telemetry and Ranging applications onboard spacecraft
Bartlomiej Mizak (1), Przemyslaw Radzik (1), Arkadiusz Byndas (1), Per Ingvarson (2), Joakim Johansson (2), Jan Zackrisson (2)
(1)Wroclaw University of Technology, Wroclaw, Poland
(2) RUAG Space, Gothenburg, Sweden

15h30-15h45
KUL and EPFL Cooperation on Numerical Integration of Sommerfeld Integrals
Vladimir Volski (1), Guy A. E. Vandenbosch (1), Athanasios Polimeridis (2), Juan R Mosig (2), Ruzica Golubovic (2)
(1) KU Leuven, Belgium
(2) EPFL, Switzerland

15h45-16h00
Revision of EBG Metamaterials and Active Antennas
Gonzalo Exposito-Dominguez (1), Jose-Manuel Fernandez-Gonzalez (2), Pablo Padilla (3), Manuel Sierra-Castaner (2)
(1) IMST Germany and UPM, Spain
(2) Universidad Politecnica de Madrid, Spain
(3) University of Granada, Spain

16h00-16h15
Thermal Calculation Using a 3D-EM Solver and Thermal-Electrical Analogy
Ismael Nistal (1), Andreas Bettray (2), Kai Maulwurf (2)
(1) U. of Carlos III, Madrid, Spain and IMST Germany
(2) IMST GmbH, Germany

SHORT COMMUNICATIONS

16h15-16h20
Numerical analysis of metamaterial barrier for integration into microstrip circuits
Przemyslaw Gorski (1), Guy Vandenbosch (2), Vladimir Volski (2)
(1)Wroclaw University of Technology, Wroclaw, Poland
(2) ESAT-TELEMIC, Katholieke Universiteit Leuven, Belgium

16h20-16h25
Time-Domain Surface Impedance of a Plasmonic Half-Space
Martin Stumpf (Katholieke Universiteit Leuven, Belgium), Guy A. E. Vandenbosch (Katholieke Universiteit Leuven, Belgium)

16h25-16h30
Common-Mode Rejection in a Connected Array of Dipoles with Inherent Frequency Selectivity Properties
Lorenzo Cifola (1), Daniele Cavallo (2), Giampiero Gerini (2), Silvio Savoia (1), Antonio Morini (1), Giuseppe Venanzoni (1)
(1) Università Politecnica delle Marche, Ancona, Italy
(29 TNO, Defense Security and Safety, The Hague, Netherlands

16h30-16h35
Mode Matching Method for the Analysis of Substrate Integrated Waveguides
M. Casalleti (1), S. Maci (1), R. Sauleau (2)
(1) U. of Siena, Italy (2) U. of Rennes, France

High Resolution Two-Dimensional DOA Estimation Using Artificial Neural Networks

Marija Agatonovic, Zoran Stanković, Bratislav Milovanović
Faculty of Electronic Engineering, University of Niš
Aleksandra Medvedeva 14, 18000 Niš, Serbia
marija.agatonovic@elfak.ni.ac.rs

***Abstract*—This paper presents an application of artificial neural network (ANN) based smart antenna in two-dimensional direction-of-arrival (2-D DOA) estimation. Data model based on the uniform rectangular array (URA) configuration is utilized for ANN modeling. It is shown that appropriately trained ANNs can be successfully used to localize narrowband sources in both the azimuth and elevation planes. In order to increase the angular resolution of 2-D DOA estimation a Two-Stage Sectorized Neural Network (TSS-NN) model is presented. By avoiding complex calculations the proposed approach is suitable for real-time applications demonstrating the accuracy that is comparable to the super-resolution 2-D MUSIC algorithm.**

Keywords-ANNs; DOA estimation; MLP; smart antennas; URA

I. INTRODUCTION

Direction-of-arrival (DOA) estimation using multiple-antenna technologies, such as smart antenna systems, is a very important problem in many applications including radar and sonar signal processing, communications and acoustics. Signals received by the individual antenna elements are down-converted into baseband signals, digitalized, and then used to form a spatial covariance matrix that is the input to most direction-of-arrival algorithms. In mobile communications, once the direction of a user is estimated this information can be forwarded to an adaptive beamforming algorithm that optimizes the radiation pattern of the antenna array. It allocates the main beam toward the user of interest and generates deep nulls in the directions of interfering signals from mobile users in adjacent cells. Namely, spatial filtering is realized, enabling the communication system to easily localize and track the user.

Subspace based estimation methods have attracted the most interest and among them, MUSIC (MUltiple SIgnal Classification) [1] and ESPRIT (Estimation of Signal Parameters via Rotational Invariance Techniques) [2] are well-known of their super-resolution capabilities. By performing spectral search MUSIC is able to provide accurate DOA estimation at the expense of high computational complexity. When multidimensional parameter estimation is required, ESPRIT demonstrates significant advantage over MUSIC. Avoiding the orthogonally search, the computational complexity of ESPRIT grows linearly with dimension, while that of MUSIC grows exponentially [3]. If a number of omnidirectional-types linear arrays are arranged one next to the other then the rectangular arrays are formed allowing both azimuth and elevation angles to be resolved. However, due to the increased dimensionality a time-consuming process of spatial covariance matrix eigenvalue decomposition (EVD) hinders the real-time use of subspace based algorithms such as 2-D MUSIC and 2-D ESPRIT.

On the other side, there are many publications on the application of artificial neural networks (ANNs) in DOA estimation of both narrowband and wideband signals [4]-[11]. Most of them report results on Radial Basis Function Neural Network (RBF-NN) modeling to estimate the DOA in the azimuth plane only, but there are also papers addressing 2-D DOA estimation [12]-[14]. Compared to conventional signal processing algorithms that are mainly based on linear models, ANNs consider DOA estimation as a function approximation problem. With the ability to map the dependence between two data sets, parameters of ANNs are optimized through the learning process in order to have outputs that are as close as possible to the desired values. To exploit ANNs in the DOA estimation problem mapping between the spatial covariance matrix and DOAs is considered and modeled. In this work Multi-Layer Perceptron (MLP) neural networks are trained to estimate 2-D DOA. A procedure to provide high-resolution DOA estimation of a source signal in both the azimuth and elevation planes is presented. The observed space is separated into sectors and neural networks for each sector are trained to detect a source and then, to estimate its DOA [6]. However, different training sets are used to train the neural networks in two stages of one sector. First, data taken with coarse steps are used to train the networks in the detection stage. After that, for the source belonging to the certain sector, more precise training data are used to develop the network in the estimation stage resulting in a highly accurate DOA estimate. The increased resolution capability enables the identification of source signals in [-90°- 90°] azimuth and [0°- 90°] elevation range.

The paper is organized as follows. In Section II the data model based on the geometry of uniform rectangular array (URA) is given. In Section III the architecture of the MLP neural network and the corresponding training procedure are described, followed by pre-processing of data for the MLP neural network training in Section IV. The results obtained from the modeling using one MLP neural network and the proposed Two-Stage Sectorized Network (TSS-NN) models are discussed in Section V. The last section contains the concluding remarks.

II. DATA MODEL

Let us consider a uniform rectangular array (URA) consisting of $M \times N$ omnidirectional elements as shown in Fig. 1. Each antenna element is denoted with (m,n), where m=0,1,...,M-1 and n=0,1,...,N-1. Elements of the URA are placed in the x and y directions with constant inter-element spacing of dx and dy, respectively. To avoid spatial aliasing, distance between adjacent elements in the URA is usually taken to be half a wavelength $d_x = d_y = \lambda/2$.

A spherical coordinate system is used to represent the directions of arrivals of the incoming plane waves. The number of K narrowband plane waves, centered at frequency ω_0, impinges on the uniform rectangular array from directions $\{(\varphi_1,\theta_1),(\varphi_2,\theta_2),...,(\varphi_K,\theta_K)\}$ in the azimuth and elevation planes, respectively. The signal received by the URA can be written as

$$\mathbf{X}(t) = \mathbf{A}(\varphi,\theta)\mathbf{S}(t) + \mathbf{N}(t), \tag{1}$$

where $\boldsymbol{X}$(t), $\boldsymbol{N}$(t), and $\boldsymbol{S}$(t) are given by

$$\begin{aligned} \mathbf{X}(t) &= [x_1(t)\ \ x_2(t)\ \ ...\ \ x_{MN}(t)]^T \\ \mathbf{N}(t) &= [n_1(t)\ \ n_2(t)\ \ ...\ \ n_{MN}(t)]^T \\ \mathbf{S}(t) &= [s_1(t)\ \ s_2(t)\ \ ...\ \ s_K(t)]^T. \end{aligned} \tag{2}$$

$\boldsymbol{X}$(t) is a vector of antenna array outputs, $\boldsymbol{N}$(t) denotes the noise vector since signals incident to the antenna array are assumed to have some noise associated with them, and $\boldsymbol{S}$(t) represents the vector of source signals.

For far-field incident signals, there are wave path-differences of antenna array elements when incident signals arrive at the receiving antenna array. Path differences cause the phase differences which are used to calculate the DOAs of the incident signals.

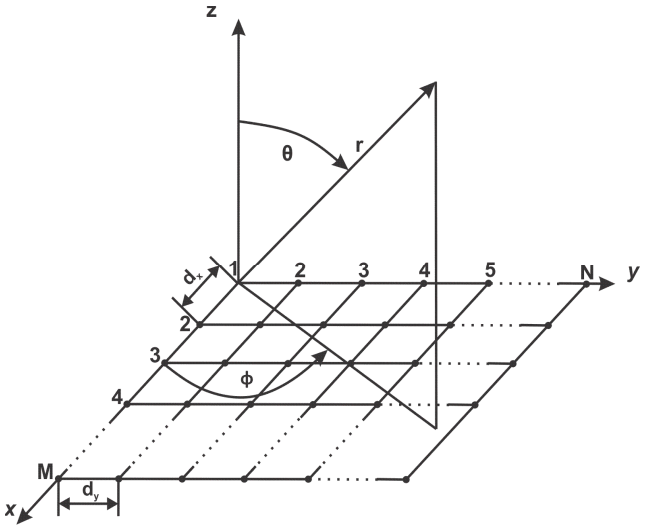

Figure 1. Uniform rectangular array (URA)

If the phase reference point is located at (m=0, n=0), the phase of the k-th incident wave at the element with the coordinates (m,n) can be determined as follows

$$\Phi_{m,n}^{(k)}(\varphi_k,\theta_k) = \frac{2\pi}{\lambda}(d_x m \sin\theta_k \cos\varphi_k + d_y n \sin\theta_k \sin\varphi_k). \tag{3}$$

Therefore, the steering vector of the k-th incident wave is given by

$$\boldsymbol{a}_{m,n}^{(k)}(\varphi_k,\theta_k) = e^{j\phi_{m,n}^{(k)}(\varphi_k,\theta_k)}, \tag{4}$$

where m=0,1,..., M-1, n=0,1,...,N-1 and k=1,2,...,K. $\boldsymbol{A}(\varphi,\theta)$ is a steering matrix whose columns are steering vectors towards K different directions of arrival, and can be written as

$$\mathbf{A}(\varphi,\theta) = [\boldsymbol{a}(\varphi_1,\theta_1)\ \ \boldsymbol{a}(\varphi_2,\theta_2)\ \ ...\ \ \boldsymbol{a}(\varphi_K,\theta_K)]. \tag{5}$$

In practice, the spatial covariance matrix $\boldsymbol{R}$ is unknown and is estimated from the available data samples x(t). If the observation period consists of P snapshots then $MN \times P$ matrix can be formed as follows

$$\begin{bmatrix} x_1^{i=1} & x_1^{i=2} & ... & x_1^{i=P} \\ x_2^{i=1} & x_2^{i=2} & ... & x_2^{i=P} \\ . & . & ... & . \\ x_{MN}^{i=1} & x_{MN}^{i=2} & ... & x_{MN}^{i=P} \end{bmatrix} = A \begin{bmatrix} s_1^{i=1} & s_1^{i=2} & ... & s_1^{i=P} \\ s_2^{i=1} & s_2^{i=2} & ... & s_2^{i=P} \\ . & . & ... & . \\ s_K^{i=1} & s_K^{i=2} & ... & s_K^{i=P} \end{bmatrix} + \begin{bmatrix} n_1^{i=1} & n_1^{i=2} & ... & n_1^{i=P} \\ n_2^{i=1} & n_2^{i=2} & ... & n_2^{i=P} \\ . & . & ... & . \\ n_{MN}^{i=1} & n_{MN}^{i=2} & ... & n_{MN}^{i=P} \end{bmatrix}. \tag{6}$$

Finally, the covariance matrix of the received noisy signals can be estimated by

$$\begin{aligned} \mathbf{R} = E\{\mathbf{X}(t)\mathbf{X}(t)^H\} &= \mathbf{A}E[\mathbf{S}(t)\mathbf{S}(t)^H]\mathbf{A}^H + E[\mathbf{N}(t)\mathbf{N}(t)^H] \\ &= \mathbf{A}R_{xx}\mathbf{A}^H + \sigma^2\mathbf{I} = \sum_{i=1}^{K} \lambda_i e_i e_i^H. \end{aligned} \tag{7}$$

In (7), $\mathbf{R}_{xx} = E[(\mathbf{S}(t)\mathbf{S}^H(t))]$ stands for the correlation matrix of the received signals, λ_i are eigenvalues of matrix $\boldsymbol{R}$, σ^2 is variance of the statistically independent white noise signals, and H denotes the conjugate transpose. According to (1) - (7), it can be observed that the antenna array performs the mapping $G: \mathbf{R}^K \rightarrow \mathbf{C}^{MN}$ from the space of DOAs, $\Phi = [(\varphi_1,\theta_1),(\varphi_2,\theta_2),...,(\varphi_K,\theta_K)]^T$ to the space of the antenna array outputs $\{\mathbf{X}(t) = [x_1(t)\ \ x_2(t)\ \ ...\ \ x_{MN}(t)]^T\}$.

III. ARTIFICIAL NEURAL NETWORKS

The architecture of a neural network used in the 2-D DOA estimation is shown in Fig 2. The neural network type is Multi-Layer Perceptron (MLP) that belongs to feed-forward neural networks. It consists of a number of basic processing units called neurons. Neurons are organized into layers such that

every neuron in each layer in the network is connected to every neuron in the adjacent forward layer. No connections are permitted between the neurons belonging to the same layer. Each neuron is characterized by its activation function and bias (threshold), and each connection between two neurons by a weight factor. A neuron communicates with others by weighs, and can be activated according to the received signals [4]-[5].

An MLP neural network (MLP-NN) consists of an input layer (layer 0), an output layer (layer N_L) as well as several hidden layers. Input vectors are presented to the input layer and fed through the network that calculates the output vector. The *l*-th layer output is given by

$$Y_l = F(W_L Y_{l-1} + B_l), \tag{8}$$

where Y_l and Y_{l-1} are outputs the of *l*-th and (*l*-1)-th layers, respectively, W_L is a weight matrix between (*l*-1)-th and *l*-th layers and B_l is a bias matrix between (*l*-1)-th and *l*-th layers. Function F is an activation function of each neuron and it is chosen to be linear for the input and output layers and sigmoid for hidden layers.

The neural network learns the relationship between sets of input-output data (training sets) which characterize the problem that is modeled. First, input vectors are presented to the input neurons and output vectors are calculated. These output vectors are then compared with desired values and errors are determined. Error derivatives are calculated and summed up for each weight and bias until the whole training set has been presented to the network. These error derivatives are then used to update the weights and biases for neurons in the model. The training process proceeds until errors become lower than the prescribed values or until the maximum number of epochs ('epoch' is one processing of the whole training set) is reached. Once trained, the network is able to generalize, that means to give accurate responses to those inputs that have not been presented to the network in the training process. The test set is taken from the same distribution as the inputs used in the training set. Accuracy of the trained MLP neural network can be expressed using a correlation coefficient between reference values and network responses.

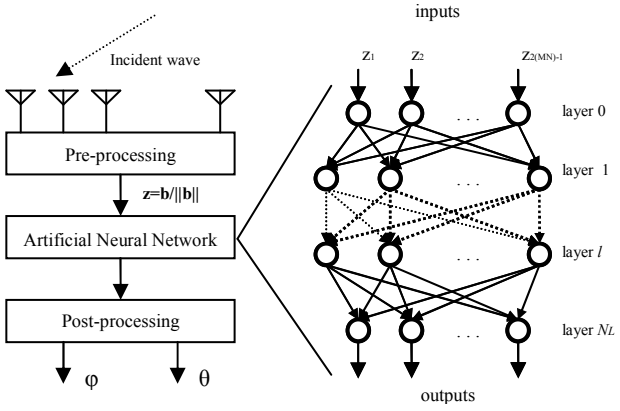

Figure 2. DOA estimation employing ANN

The Pearson Product-Moment correlation coefficient r is defined by

$$r = \frac{\sum (x_i - \overline{x_i})(y_i - \overline{y_i})}{\sqrt{\sum (x_i - \overline{x_i})^2 \sum (y_i - \overline{y_i})^2}}, \tag{9}$$

where x_i represents the reference value, y_i is the ANN computed value, $\overline{x}$ is the reference sample mean, and $\overline{y}$ is the ANN sample mean. The correlation coefficient is an indicator of how well the modeled values match the actual ones. If the correlation coefficient is close to one then the neural network has an excellent predictive ability whereas r close to zero indicates poor performance of the network. To achieve required performance of MLP-NN modeling, the number and size of hidden layers have to be determined. Since these parameters cannot be known *a priori*, they are usually determined experimentally through the training of several MLP-NNs. Finally, the MLP-NN model with the best performance is chosen for simulations and further analysis.

IV. Pre-Processing of Data for ANNs

Application of ANNs in the area of DOA estimation is based on the inverse mapping to the one that the antenna array performs. That is the mapping $G: \mathbf{C}^{MN} \rightarrow \mathbf{R}^K$ from the space of antenna array outputs $\{\mathbf{X}(t) = [x_1(t)\ x_2(t)\ ...\ x_{MN}(t)]^T\}$ to the space of DOAs $\Phi = [(\varphi_1, \theta_1), (\varphi_2, \theta_2), ..., (\varphi_K, \theta_K)]^T$. The input data of ANN is the spatial covariance matrix $\boldsymbol{R}$ of the antenna array outputs, and DOAs of users' signals are ANN responses. The number of neurons in the input layer of the network depends on the dimensionality of $\boldsymbol{R}$ matrix. Since $\boldsymbol{R}$ is an $MN \times MN$ square matrix and keeping in mind that ANNs cannot operate with complex numbers, there should be $2(MN)^2$ neurons in the input layer of the network. Since the covariance matrix depends both on the azimuth and elevation angles, separate training sets cannot be used as the network input to train only the azimuth, or only elevation. For that reason, the dimensionality of input layer significantly increases when large antenna arrays are employed at the receiving end.

In this paper, a dimension-degraded training set is used to develop MLP-NNs. Only the first row of covariance matrix is used to represent signals at the array output [8]. Therefore, all inputs are organized into a $2(MN)$-1 element vector $\boldsymbol{b}$. Before it is applied to the input layer of the neural network, the input vector $\boldsymbol{b}$ is normalized with its norm, $\boldsymbol{z} = \boldsymbol{b}/\|\boldsymbol{b}\|$. In this way, the dimensionality of input vectors is significantly reduced allowing efficient training of the neural networks.

V. Modeling Results

Computer simulations employing both one MLP-NN and the TSS-NN model are performed. For that purpose, data model based on the rectangular antenna array with 16 identical omnidirectional elements spaced half a wavelength apart is used. The spatial covariance matrix $\boldsymbol{R}$ is estimated from 1024 snapshots of BPSK modulated signal. The results were considered for signal-to-noise (SNR) ratio of 10 dB.

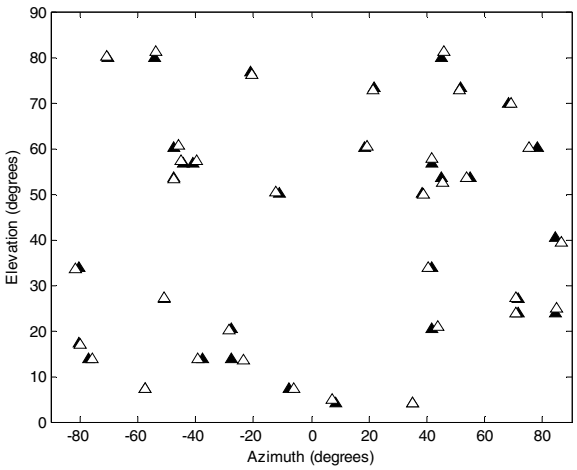

Figure 3. MLP-NN results for 35 test points compared to reference DOAs (white triangles - MLP-NN response, black triangles - reference DOAs)

A. One MLP-NN for 2-D DOA estimation

One source moving in steps of 2° is tracked in the azimuth [-90°-90°] and elevation [0°-90°] range. The input information to the MLP-NN is the first row of the spatial covariance matrix and the output is the calculated DOA of the source signal. The MLP-NN with the best performance, having two hidden layers with 18 neurons in each of them and correlation coefficient for test data of 0.9994, is chosen for simulations. A number of DOAs and the quality of the associated estimates using URA configuration is shown in Fig. 3. Data points used to test MLP-NN model have not been used in the training process. The black triangles represent the true DOAs while the white triangles represent the appropriate MLP-NN responses. It can be concluded that results provided by MLP-NN modeling are in good agreement with the actual DOAs. Since the neural network was trained with the resolution of 2° it cannot be expected to demonstrate better performance than that for which it was trained. If a higher accuracy of DOA estimation is required, a very large training set must be used to train a single neural network. The whole process can appear to be very difficult and time-consuming.

B. TSS-NN model for 2-D DOA estimation

In Fig. 4, the TSS-NN model for highly accurate 2-D DOA estimation is presented. The observed space is divided into four sectors of the same width in azimuth (45º) and elevation (90º). Each sector consists of two stages, one for the detection of the source signal and the other, for DOA estimation. The network in the detection stage is supposed to activate the corresponding network in the estimation stage if a source is present in the sector. This results in a high resolution DOA estimate. The procedure to train the MLP-NNs used in the TSS-NN model is described as follows. First, data taken with fine steps close to the borders of the sector and coarser steps towards its centre are used to train the networks in the detection stage. After that, for the source belonging to the sector, more precise data are used to train the network in the estimation stage giving as a result a highly accurate DOA estimate.

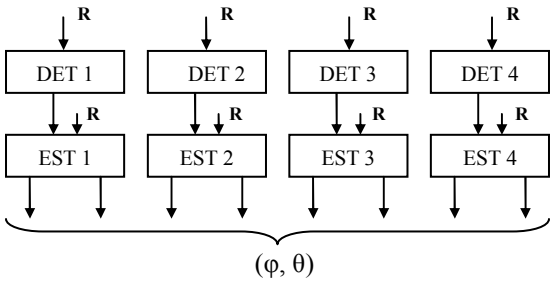

Figure 4. TSS-NN model with sectorization applied to azimuth angles

Following the previously described procedure, several smaller data sets are formed to allow efficient training of the MLP-NNs instead of one large data set, in case when only one MLP-NN is employed for 2-D DOA estimation.

The output of the MLP-NN in the detection stage is 0 when the tracked source is outside the observed sector, and 1 for the source inside the sector. The network in the detection stage of the second sector, with 12 and 10 neurons in two hidden layers, is developed and tested for points at θ=49° that have not been used in the training process. As it is demonstrated in Fig. 5, the network will activate the corresponding estimation stage to provide the DOA of the source signal in azimuth range [-45º - 0º]. For the estimation stage, MLP-NNs with two hidden layers and different number of neurons in each of them are trained. Training data are taken in steps of 0.5° in azimuth and elevation in order to increase the accuracy of DOA estimates. The MLP-NN with 12 neurons in both hidden layers has demonstrated the best performance (r=0.9997) and was chosen for simulations. Results of the TSS-NN modeling and 2-D MUSIC with the resolution of 0.5º are plotted for azimuth and elevation angles in Fig. 6 and 7. It can be concluded that the TSS-NN model has performance that is almost equal to that of the 2-D MUSIC. However, the TSS-NN model provides DOA estimates in a matter of seconds while 2-D MUSIC needs 10 s using the Intel(R) Core(TM)2 Quad CPU computer with 8 GB RAM. In Fig. 8, source locations estimated using the TSS-NN model (black triangles) are in good agreement with the actual ones (black triangles), thereby proving the performance of the proposed model.

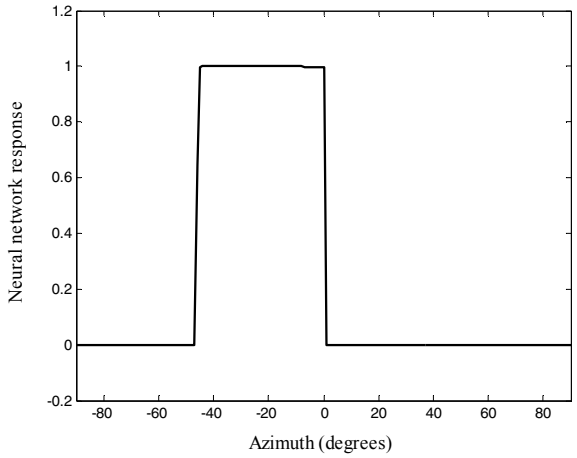

Figure 5. Response of the MLP-NN in the detection stage of the 2nd sector at θ=49º

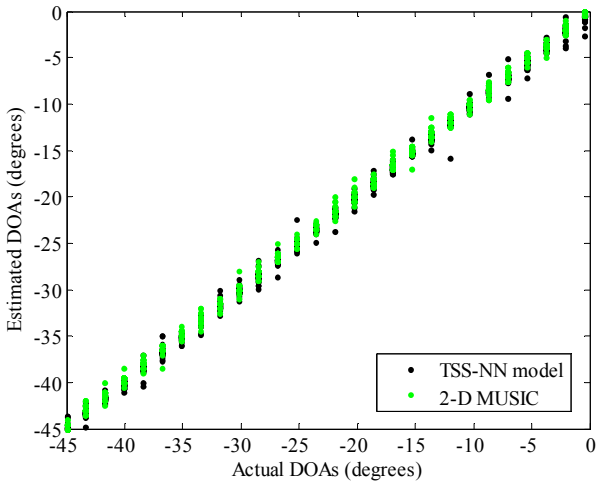

Figure 6. Correlation diagram of TSS-NN and 2-D MUSIC DOAs for azimuth angles

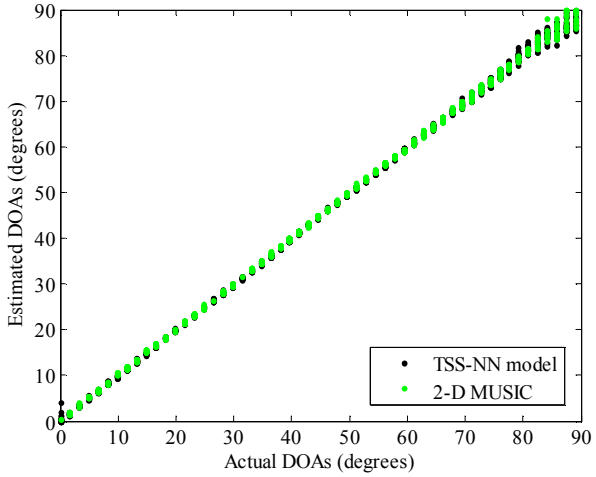

Figure 7. Correlation diagram of TSS-NN and 2-D MUSIC DOAs for elevation angles

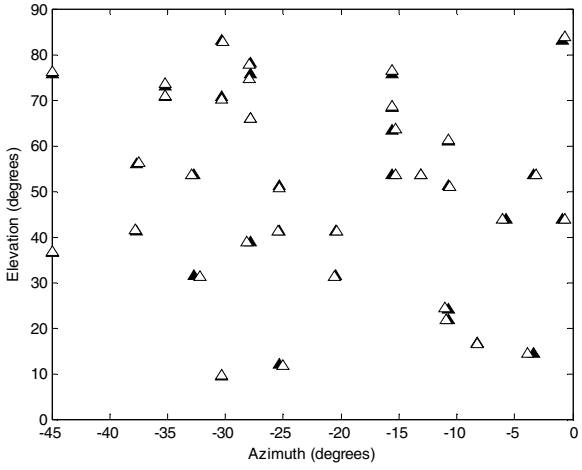

Figure 8. TSS-NN model results for 35 test points compared to reference DOAs (white triangles - TSS-NN model response, black triangles - reference DOAs)

VI. Conclusion

In this work an efficient neural network-based model for high-resolution 2-D DOA estimation is presented. The developed model consists of several MLP neural networks trained to detect a source signal and estimate its DOA. Networks are organized into sectors and smaller data sets are used to develop MLP-NNs for each of them. Results obtained from simulation experiments show that the TSS-NN model is capable of correctly identifying the DOA of the source signal in both the azimuth and elevation planes. A key advantage of this approach over the super-resolution 2-D MUSIC is its ability to provide the output response almost instantaneously making it suitable for real-time implementation.

Acknowledgement

This work was supported by the Institut für Hochfrequenztechnik und Elektronik (IHE) of Karlsruhe Institute of Technology (KIT), under the CARE framework.

References

[1] R. Schmidt, “Multiple emitter location and signal parameter estimation,” IEEE Trans. Antennas Propag., vol. 34, pp. 276-280, March 1986.

[2] R. Roy and T. Kailath, “ESPRIT-estimation of signal parameters via rotational invariance techniques,“ IEEE Trans. Acoust. Speech Signal Process., vol. 37, pp. 984 – 995, Jul 1989.

[3] B. Ottersten, M. Viberg, and T. Kailath, “Performance analysis of the total least squares ESPRIT algorithm,” IEEE Trans. on Signal Processing, vol. 39, no. 5, pp. 1122-1134, May 1991.

[4] Q. J. Zhang and K. C. Gupta, Neural networks for RF and microwave design, Artech House, July 2000.

[5] C. G. Christodoulou and M. Georgiopoulos, Application of neural networks in electromagnetics, Artech House, December 2000.

[6] A. H. El Zooghby, C. G. Christodoulou, and M. Georgiopoulos, “Performance of radial-basis function networks for direction of arrival estimation with antenna arrays,” IEEE Trans. Antennas Propag., vol. 45, no. 11, November 1997.

[7] A. H. El Zooghby, C. G. Christodoulou, and M. Georgiopoulos, "A neural network-based smart antenna for multiple source tracking," IEEE Trans. Antennas Propag., vol. 48, no. 5, May 2000.

[8] S. Çaylar, K. Leblebicioğlu, and G. Dural, "A new neural network approach to the target tracking problem with smart structure,” Proc. of IEEE AP-S International Symposium and USNC/URCI meeting, pp. 1121-1124, July 2006.

[9] M. Sarevska, B. Milovanović, and Z. Stanković, "Neural network - based DOA estimation and beamforming for smart antenna," Proc. of Conference ICEST, Sofia, Bulgaria, pp. 25-28, July 2006.

[10] M. Agatonović, Z. Stanković, B. Milovanović, and N. Dončov, “DOA estimation based on radial basis neural networks as uniform circular antenna array processor,“ Proc. of the X Conference TELSIKS, Serbia, October , 2011.

[11] M. Wang, S. Yang, S. Wu, and F. Luo, "A RBFNN approach for DOA estimation of ultra wideband antenna array," Neurocomputing-Elsevier, vol. 71, January 2008.

[12] N. Jorge, G. Fonseca, M. Coudyser, J.-J. Laurin, and J.-J. Brault, “On the design of a compact neural network-based DOA estimation system,” IEEE Trans. Antennas Propag., vol. 58, no. 2, February 2010.

[13] T. Matsumoto and Y. Kuwahara, “2-D DOA estimation using beam steering antenna by the switched parasitic elements and RBF neural network,” Electron. Comm. Jpn. 1, vol. 89, no. 9, 2006.

[14] C. Hongguang, Li biao, and S. Zhenkang,” Efficient network training method for two-dimension DOA estimation ,” Computer and Information Technology CIT '04, pp. 1028 – 1032, September 2004.

Design and Analysis of Planar UHF Wearable Antenna

Branimir Ivšić, Juraj Bartolić, Davor Bonefačić
Department for Wireless Communications
University of Zagreb, Faculty of Electrical Engineering and Computing
Zagreb, Croatia
branimir.ivsic@fer.hr

Anja Skrivervik, Jovanche Trajkovikj
Laboratory of Electromagnetics and Acoustics
Ecole Polytechnique Federale de Lausanne
Lausanne, Switzerland
anja.skrivervik@epfl.ch

Abstract— **Slotted PIFA on the textile substrate suitable for body-centric applications in the UHF band is proposed. The influence of slot in the ground plane on the antenna parameters is theoretically investigated using simplified model of human body.**

Keywords- wearable antennas, PIFA, on-body propagation, off-body propagation

I. INTRODUCTION

Since 1980s the everyday life has seen the growing use of various handheld wireless devices whose dimensions are miniaturized due to the advance in technology of fabrication of electronic components. Such progress has consequently leaded to demand for reducing the size of antennas as well, for which various techniques were proposed. As a next step the interest in body centric communications is emerging, which account to personal communication system consisting of body-worn devices which communicate with the environment ("off-body"), mutually ("on-body") and possibly with medical implants ("in-body") [1-5]. The possible use of body-centric devices has a broad range – they could be used for military, rescue, medical or entertaining purposes. Given that such system is intended to be used on the daily basis, its components should not be obtrusive and not affecting other activities of the user. Since antenna is a necessary part of any such device, the recent research activities in that area are focused to antenna-human interaction and demand to design antennas that are light-weight, flexible, conformable to the body while at the same time maintaining good radiation efficiency and reduced radiation towards the body. Such demands are contradictory so usually compromises are needed. As a good candidate planar antennas using clothing as substrate have been proposed (so-called wearable or textile antennas) and thus conventional wearable antennas are planar dipoles and monopoles, or patch antennas (with or without modifications) [5]. The latter are of particular interest since they possess reduced radiation towards human body due to the presence of the ground plane and the techniques of size reduction [6] are generally applicable (although possibly at the cost of increased radiation towards body). They can thus be considered as a good trade-off between aesthetical and functional point of view.

II. THE PROPOSED ANTENNA

Our research was focused on the body-centric communications in the UHF range (in particular, around 400 MHz) and the goal was to design proper wearable textile antenna for that range. Such antenna is in principle intended for medium range off-body communications, which could be useful e.g. for rescue and military teams.

Using the commercial software CST Microwave Studio the antenna based on a PIFA concept (which is commonly exploited in GSM communications) has been designed and optimized for operation around 400 MHz in free space. The design itself was inspired by [7]. As a substrate, 4 mm thick fleece (relative permittivity of 1.1) was used, which is quite thin in terms of the wavelength in the UHF frequency range. The proposed antenna consists of the ground plane with slot, slotted patch and shorting wall (S.W.), as shown on Fig.1. The slots were introduced to reduce the antenna dimensions and improve the bandwidth while in the first case the patch was placed along one edge of the ground plane, i.e. asymmetrically. The slot in the ground plane was placed at the 80 mm distance from the shorting wall, beneath the patch, while the feeding point was placed at the 49.5 mm distance from the shorting wall (it was recalculated later when needed). The dimensions of the antenna components are summarized in Table 1.

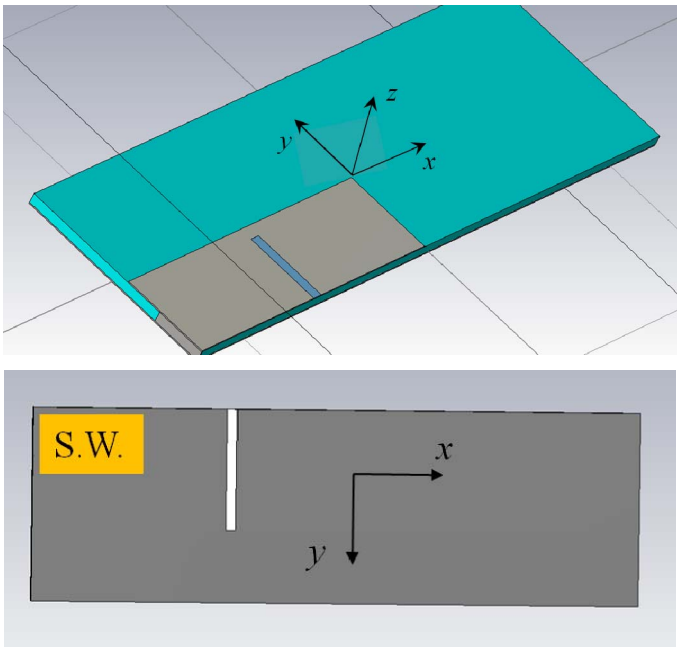

Figure 1. The proposed PIFA – top and bottom view

After designing the antenna in free space, its performance was checked in the vicinity of the human body model. As a simplified body model a rectangular lossy dielectric box of dimensions 45×40×18 cm has been used. The relative permittivity and conductivity were taken corresponding to the muscle tissue at 400 MHz and amounted 57.129 and 0.8, respectively (loss tangent turns to be 0.626) [8]. Such model corresponds to the body trunk and the antenna was placed in the middle of its largest face (corresponding to e.g. chest).

TABLE I. DIMENSIONS OF PROPOSED PIFA IN [MM]

Ground plane size	250 × 80
Patch length	120
Patch width	35
Shorting wall length	20
Ground plane slot length	50
Patch slot length	30
Slot width	4

When placed on the body model, the resonant frequency shifted upwards by 21% (i.e. to around 500 MHz), as shown in Fig. 2. Such unexpected up-shift in frequency was confirmed by simultaneous simulations in Ansoft HFSS. In addition, as qualitatively shown in Figs. 3 and 4, most of the field on the ground plane for the case with body was concentrated mostly around the patch region (i.e. part of ground plane further from patch had very low magnitudes) suggesting the antenna in the presence of the body appears to be electrically shorter. Furthermore, part of ground plane placed further from patch appears redundant in terms of surface currents, suggesting some further reduction in size of the ground plane is possible.

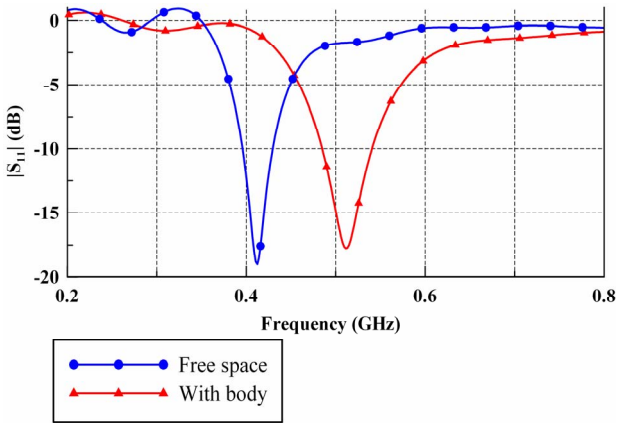

Figure 2. Input reflection coefficient vs. frequency for proposed antenna

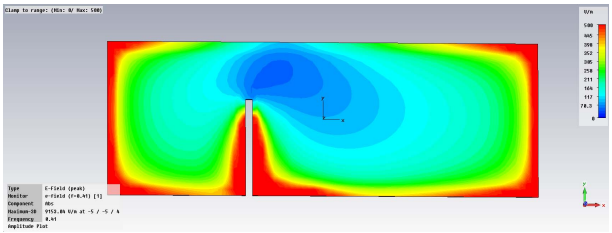

Figure 3. Magnitude of the electric field on the ground plane in free space

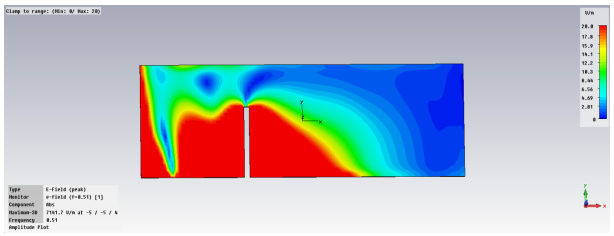

Figure 4. Magnitude of the electric field on the ground plane with body model

In the presence of the human body model radiation efficiency plummeted to -17 dB, leading to a gain of around -13 dBi. Such low value of the radiation efficiency is not unusual in the relevant literature, meaning there is significant influence of the body to the antenna performance.

III. FURTHER ANALYSIS

A. Position of the slot in the ground plane

When the slot was removed from the ground plane, resonant frequency was around 500 MHz for both free space case and with body model. Furthermore, radiation efficiency with body model was 10 dB higher (although bandwidth was reduced). This means the slot in the ground plane interacts with the antenna near field and alters its radiation properties as well as largely contributes to coupling with the body (apart from diffraction from finite ground plane).

In subsequent simulations changing of the length and position of the slot in the ground plane was performed in order to investigate slot influence to the antenna performance. As expected, by increasing the length of the slot in free space the resonant frequency was getting lower (and the proper feeding point was altered). When the body model was present, the influence of slot length to the resonant frequency and matching was less pronounced.

The position of the slot also influences the resonant frequency and matching in free space, as shown in Fig.5. The resonant frequency is lower when the slot is placed closer to the shorting wall, which means stronger influence is obtained there. Also the feeding point is changed, i.e. mismatch occurred for some cases. When placed on the body (Fig. 6) the effect of the slot again generally diminishes, however stronger influences for the cases when slot is put between shorting wall and feeding point (R=20 and 40 mm) were observed, suggesting some additional resonances occur. Still, here needs to be noted that in HFSS actually different results were obtained for the respective slot distances, meaning some more explanation is needed.

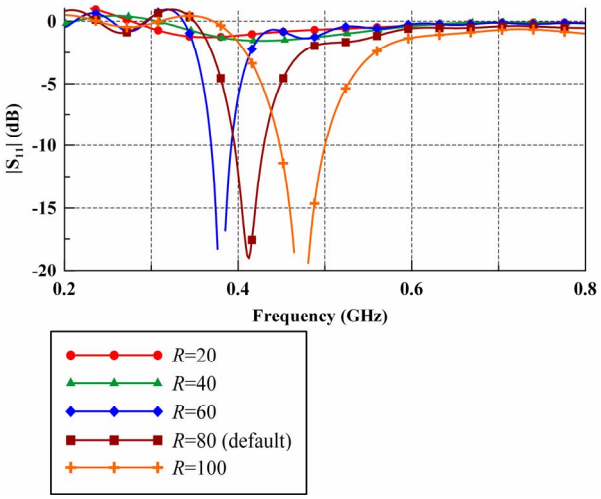

Figure 5. Input reflection coefficient for various distances R of the ground plane slot from the shorting wall – free space

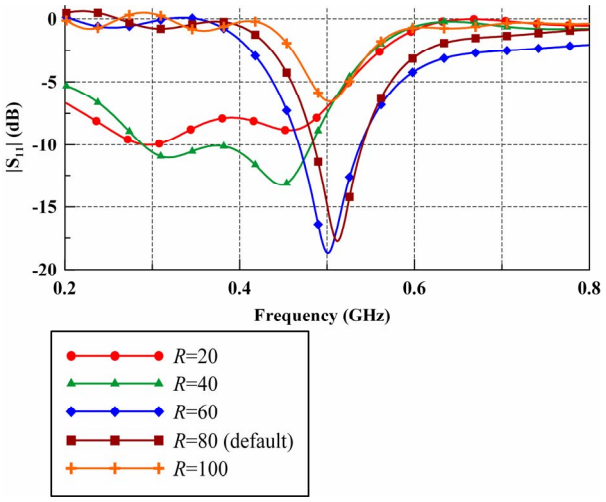

Figure 6. Input reflection coefficient for various distances R of the ground plane slot from the shorting wall – with body model

The influence of the patch position on the ground plane was also investigated, as shown in Table II. By moving the patch away from the edge of the ground plane it was found that it is possible to improve the radiation efficiency by up to around 7 dB. The effect was observed even when the patch was moved closer to the other edge, meaning that the improvement in efficiency in fact occurs by leaving part of ground plane slot open. This suggests that the patch and the ground plane form a capacitor through which, when a slot is placed, the antenna near field couples more into the body thereby reducing radiation efficiency. The more the slot was uncovered the more such coupling has been reduced.

TABLE II. INFLUENCE OF PATCH POSITION ON PIFA PARAMETERS

Distance from the edge [mm]	Rad. efficiency [dB]	Resonant frequency [GHz]	BW [%]
0 (default)	-16.98	0.511	10.78
10	-15.95	0.504	7.2
20	-13.15	0.484	3.54
30	-10.18	0.487	2.1

B. *Symmetric PIFA*

As an illustration we consider the case where the patch was moved to the middle of the ground plane along ground plane width, i.e. placed symmetrically (Fig. 7). For this case patch distance from the edge was 22.5 mm. The radiation efficiency was around -12 dB, which is improvement of 5 dB compared to PIFA placed along the edge of ground plane. On the other hand, the observed frequency up-shift (compared to free space) was only around 2%. Therefore when the part of slot in ground plane is open, the effect of the slot in ground plane on the resonant frequency is considerably lower, as described before.

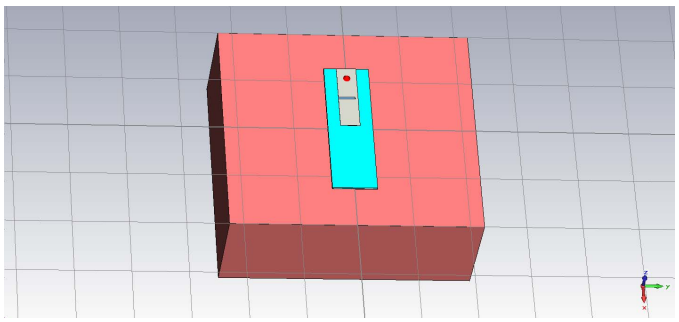

Figure 7. PIFA with symmetrically placed patch on body - illustration

For the case of symmetrically placed patch the influence of each slot (in the ground plane and in the patch, respectively) on the antenna performance was separately analyzed in some more details. The relevant results are shown in Table III, while in Table IV the radiation efficiency and gain for considered cases are summarized.

By analyzing the results it can be observed that the presence of slot in the ground plane contributes to radiation bandwidth and couples to the body causing the already observed up-shift in resonant frequency. On the other hand, the slot in the patch merely lowers the resonant frequency (both in free space and with body model) making the antenna appear electrically larger and has no significant effect on the coupling with body.

TABLE III. INFLUENCE OF EACH RESPECTIVE SLOT IN PIFA

	f_r - free space	f_r - with body	BW-free space	BW-with body
No slots	0.551 GHz	0.549 GHz	2.18 %	1.27 %
Only ground plane slot	0.531 GHz	0.549 GHz	6.59 %	8.62%
Only patch slot	0.486 GHz	0.484 GHz	2.67 %	1.03 %
Both slots	0.475 GHz	0.484 GHz	5.68 %	3.72 %

TABLE IV. RADIATION EFFICIENCY AND GAIN

	Rad. efficiency [dB]	Gain [dBi]
No slots	-5.551	-0.859
Only ground plane slot	-11.55	-6.889
Only patch slot	-7.085	-3.019
Both slots	-12.27	-8.231

To illustrate coupling with the human body, in Fig. 8 power flow in E-plane is depicted. It can be seen that the coupling occurs through the slot and through the edge of the ground plane where a shorting wall is present. The latter coupling mechanism was attempted to be reduced by adding some more ground plane behind the shorting wall (i.e. effectively translating the patch and the slot), which is shown in Fig. 9. Nevertheless, virtually no improvement in radiation efficiency was obtained for this case.

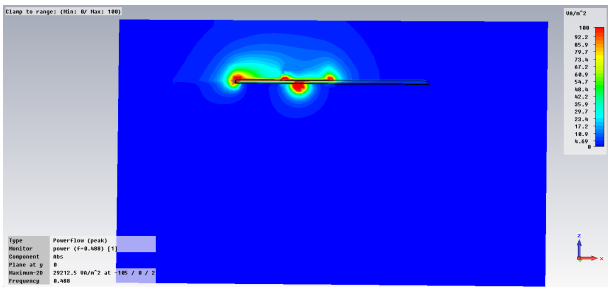

Figure 8. Power flow in E-plane

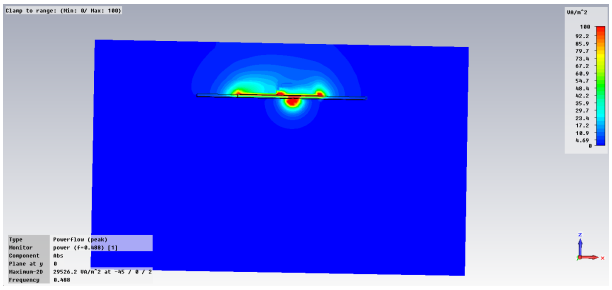

Figure 9. Power flow in E-plane for translated patch

IV. THE FUTURE WORK

The future work would focus on theoretical description of radiation mechanism of the PIFA in the presence of the human body (e.g. in terms of equivalent circuit) as well as the study of the interaction of slot in the ground plane and slot in the patch. Improvements of radiation efficiency and possible further reduction in size (e.g. by adding more slots in the patch) as well as feeding arrangements that are most suitable to be worn on the clothes are also to be considered. In order to verify the results of simulations, fabrication of the prototype and measurements in free space and in presence of the body phantom will be performed. Finally, antenna coupling when two or more antennas are placed on the human body would be investigated.

[1] N. H. M. Reis et al., "A review of wearable antenna", in Proceedings of Antennas and propagation conference 2009, pp. 225–228, Loughborough (UK), 2009

[2] P. S. Hall and Y. Hao, "Antennas and propagation for body-centric communications", in Proceedings of EuCAP 2006, pp. 1–7, Nice (France), 2006

[3] P. S. Hall, Y. Hao and S. L. Cotton, "Advances in antennas and propagation for body-centric wireless communications", in Proceedings of EuCAP 2010, pp. 1–7, Barcelona (Spain), 2010

[4] J. C. G. Matthews and G. Pettitt, "Development of flexible, wearable antennas", in Proceedings of EuCAP 2009, pp. 1–7, Berlin (Germany), 2009

[5] P. S. Hall and Y. Hao (eds), "Antennas and propagation for body-centric wireless communications", Artech house, 2006

[6] A. K. Skrivervik, J.-F. Zürcher, O. Staub, J.R. Mosig, "PCS antenna design: The challenge of miniaturization", IEEE Antennas and Propagation Magazine, Vol. 43, No. 4, pp. 12–26, August 2001.

[7] M. Cabedo-Fabres, E. Antonino-Daviu, A. Valero-Nogueira, M. F. Bataller, "The theory of characteristic modes revisited: A contribution to design of antennas for modern applications", IEEE Antennas and Propagation Magazine, Vol. 49, No. 5, pp. 52 – 68, October 2007

[8] (2011) An Internet resource for calculation of dielectric parameters of body tissues.[Online]. Available: http://niremf.ifac.cnr.it/tissprop/

KUL and EPFL Cooperation on Numerical Integration of Sommerfeld Integrals

Vladimir Volskiy, and Guy A. E. Vandenbosch
Katholieke Universiteit Leuven,
ESAT-TELEMIC,
Leuven, Belgium
vladimir.volski@esat.kuleuven.be
guy.vandenbosch@esat.kuleuven.be

Athanasios G. Polimeridis, Juan R. Mosig and Ruzica Golubović Nićiforović
Ecole Polytechnique Fédérale de Lausanne (EPFL),
Laboratory of Electromagnetics and Acoustics (LEMA)
Lausanne, Switzerland
ruzica.golubovic@epfl.ch
athanasios.polymeridis@epfl.ch
juan.mosig@epfl.ch

Abstract—**This paper reports the result of the cooperation between KUL and EPFL on the numerical integration of Sommerfeld integrals (SI). Each institution is well-known for developing specific techniques suited for the evaluation of SI: double-exponential quadrature rules to take the tail of the integral into account (EPFL) and an asymptotic extraction technique to remove the singularities (KUL). The combination of these two techniques results in a very promising algorithm, allowing to perform the integration along the real axis only. Several examples illustrate the algorithm efficiency.**

Keywords: Sommerfeld integrals, singularities, Green's functions

I. INTRODUCTION

The design and analysis of antennas and circuit elements embedded in multilayered structures can be performed very efficiently using the combination of a Mixed Potential Integral Equation (MPIE) with the Method of Moments (MoM). This approach requires a fast and accurate computation of the associated Green's functions in spatial domain, commonly called Sommerfeld integrals (SIs):

$$S_n\left\{\widetilde{G}\left(k_\rho,z,z'\right)\right\}=\frac{1}{2\pi}\int_0^\infty \widetilde{G}\left(k_\rho,z,z'\right)J_n\left(k_\rho\rho\right)k_\rho dk_\rho \qquad (1)$$

where $\widetilde{G}$ is the spectrum of the Green's function, k_ρ is the spectral parameter, ρ is the radial distance between the source and the observation points, and J_n is the Bessel function of the first kind and of order n. A typical behavior of the spectrum $\widetilde{G}$ is shown in Fig. 1. The direct evaluation of (1) encounters a lot of problems due to the complex behavior of the different factors in the integrand. The main problems are

1. slow decay of $\widetilde{G}$ and Bessel functions resulting in a bad convergence,
2. oscillations introduced by the Bessel function which are becoming prohibitively high for large ρ- values ,
3. different spectral singularities (poles and branch point) lying on the real axis or in its vicinity.

Several methods used to avoid these problems are mentioned in Table 1.

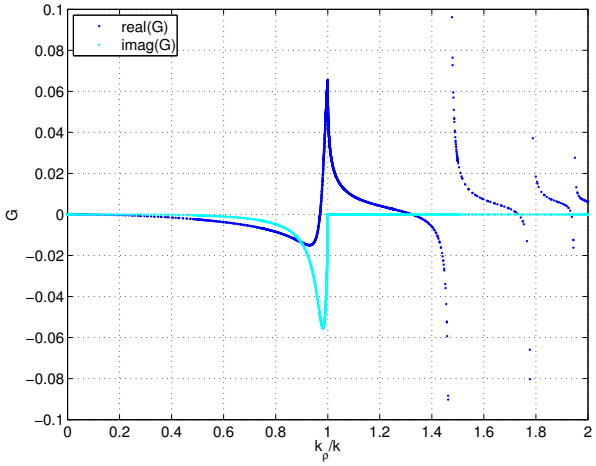

Fig. 1. Spectrum of Green's function (ε=4, f=8 GHz, h=3/80 m).

Table 1. Special techniques for the evaluation of Green's functions.

Institution	Branch point and Singularities	Tails	Large distances
Typical approach	Contour deformation	Free space asymptotes	asymptotes + integration points +++
EPFL	Contour deformation	double-exponential quadrature rules	double-exponential quadrature rules
KUL	Annihilating functions	Special asymptotes	Expansion wave concept

The most common way to avoid problems coupled with the singularities and the branch point consists of the deformation

This work was supported by the Secondments Program in the FP7 CARE project.

of the integration path. The bad convergence can be improved using free space asymptotes and the Kummer transformation.

In this paper the result of the on-going cooperation between KUL and EPFL in the evaluation of SI is reported. Each institution develops specific techniques suited for the efficient evaluation of the SI (marked by a color in Table 1):
- double-exponential quadrature rules to take the tail of the integral into account (EPFL)
- an asymptotic extraction technique to remove the singularities (KUL).
This cooperation started within the FP7 CARE project. There was a double 2 weeks exchange of researchers giving a unique opportunity of forming a deep common understanding of the advantages of each approach. Ruzica Golubovic from EPFL visited KUL in November 2010 and Vladimir Volski was at EPFL in May 2011.

II. THEORY

Recently, a novel technique has been proposed by EPFL for the direct integration of this SI tail, based on double-exponential (DE) quadrature formulas [3]. Compared to the integration-then-summation approach combined with the weighted average method, the proposed method [3] maintains the high accuracy, while reducing the overall computational cost. However this method cannot be directly applied to the whole SI because of the aforementioned singularities (poles and branch point). If the surface wave poles and branch point singularities are extracted from the spectral domain Green's functions, the complete integration could be performed along the real-axis, overcoming the limitations of the deformed-path procedure. This extraction can be performed using the techniques developed by KUL in [4-6].
The behavior of the Green's function spectrum in the proximity of the singularities can be annihilated by specially selected annihilating functions. The function parameters around the poles (position and residue) can be estimated numerically with a very high accuracy using standard algorithms. Around the branch point (*K*) the Green's function spectrum can be expanded in γ-series ($\gamma = \sqrt{k_\rho^2 - K^2}$) using a combination of different Taylor series or a simple numerical fitting. Further, the functions selected should satisfy the following requirements:

1. the behavior around the singularity in spectral domain should be similar to the behavior of the original Green's function,
2. an annihilating function should introduce no extra singularities,
3. it should also have a sufficiently fast decay for large k_ρ in order not to generate any singularity in spatial domain at the origin ρ=0,
4. the function should be known in closed form in spectral and spatial domains.

In this way, the problematic behaviors due to the poles and the branch point are extracted in spectral-domain, leading to a smoother spectral-domain Green's function, which can be efficiently integrated over the interval (0,∞) along the real axis only. The integral is split into two parts due to a different integrand behavior for small and large k_ρ values.

In practice, this annihilation procedure can be expressed using the following formulas:

$$G(\rho) = \int_{\sim 0}^{+\infty} \left[\tilde{G}(k_\rho, z, z') - \tilde{G}_{AF}(k_\rho, z, z') \right] J_0(k_\rho \rho) k_\rho dk_\rho + G_{AF}(\rho)$$
$$G_{AF}(\rho) = \int_{\sim 0}^{+\infty} \left[\tilde{G}_{AF}(k_\rho, z, z') \right] J_0(k_\rho \rho) k_\rho dk_\rho. \quad (2)$$

The function parameters around the poles (position and residue) can be estimated numerically with a very high accuracy using standard algorithms. Around the branch point (*K*) the Green's function spectrum can be expanded in γ-series ($\gamma = \sqrt{k_\rho^2 - K^2}$) using a combination of different Taylor series.
The proposed approach can be used for both single and multi layered structures without any special modifications. For convenience and in order to illustrate all steps in detail, we consider an infinitesimal horizontal electric dipole (HED) located on the top of a grounded dielectric slab with the permittivity ε and the thickness h. The parameters of the structure used in the calculation are ε=4, f=8 GHz and h=3/80 m.

TABLE I. SPECTRAL ASYMPTOTIC BEHAVIOR.

Spectral Asymptotic behavior	Singular Spatial behavior
$e^{-k_\rho \Delta} / k_\rho^3$	$R \ln R - R$
$e^{-k_\rho \Delta} / k_\rho^2$	$\ln R$
$e^{-k_\rho \Delta} / k_\rho$	$\frac{1}{R}$
$e^{-k_\rho \Delta}$	$\frac{1}{R^2}$
$k_\rho e^{-k_\rho \Delta}$	$\frac{1}{R^3}$

where $R = \sqrt{\rho^2 + \Delta^2}$

An example of the Green's function spectrum for this structure can be expressed in the following form:

$$\tilde{G}(k_\rho) = \frac{1}{\gamma}\left(1 + \frac{R - e^{-\gamma_\varepsilon h}}{1 - \mathrm{R} e^{-\gamma_\varepsilon h}}\right),$$
$$R = \frac{\gamma - \gamma_\varepsilon}{\gamma + \gamma_\varepsilon};\ \gamma = \sqrt{k_\rho^2 - K^2},\ \gamma_\varepsilon = \sqrt{k_\rho^2 - \varepsilon K^2}. \quad (3)$$

Around the branch point ($k_\rho = K$) the Green's function spectrum can be expanded in the γ series. It should be noted that the spectrum is expressed in terms of the spectral

parameter k_ρ and not γ. A direct way to find expansion coefficients using the formula for Taylor series is very cumbersome because it involves the calculation of multiple higher order derivatives. An alternative approach consists in a several steps procedure. At first all spectral parameters are expressed in terms of γ and then expansions of different functions in Taylor series are used. The two spectral parameters k_ρ and γ are coupled by the following relations:

$$\gamma = \sqrt{k_\rho^2 - K^2}, k_\rho = \sqrt{\gamma^2 + K^2}. \quad (4)$$

The spectral propagation constant in the layer is

$$\gamma_\varepsilon = \sqrt{k_\rho^2 - K^2\varepsilon} = \sqrt{\gamma^2 + K^2(1-\varepsilon)}. \quad (5a)$$

It can be rewritten in a more suitable form

$$\gamma_\varepsilon = \sqrt{1-\varepsilon}K\sqrt{1+\frac{1}{(1-\varepsilon)K^2}\gamma^2}. \quad (5b)$$

Then the Taylor expansion of $\sqrt{1+x}$ around x = 0 can be used

$$\gamma_\varepsilon \approx \sqrt{1-\varepsilon}k\left(\begin{array}{l} 1+\frac{1}{2}\frac{1}{1-\varepsilon}\frac{\gamma^2}{k^2}-\frac{1}{8}\left(\frac{1}{1-\varepsilon}\right)^2\frac{\gamma^4}{k^4} \\ +\frac{1}{16}\left(\frac{1}{1-\varepsilon}\right)^3\frac{\gamma^6}{k^6}+\ldots \end{array}\right) \quad (6)$$

As expected the expansion of the γ_ε is continuous around the branch point because it contains only the even powers of γ. In a similar way other expansions can be derived in a numerical way keeping only the required power of γ. The most important expansions are

$$\lim_{\gamma\to 0} e^{\sum_{n=0}^{N} c_n\gamma^n} \approx \sum_{n=0}^{N} d_n\gamma^n,$$

$$\lim_{\gamma\to 0} \frac{\sum_{n=0}^{N} a_n\gamma^n}{\sum_{n=0}^{N} b_n\gamma^n} \approx \sum_{n=0}^{N} d_n\gamma^n, \quad (7)$$

$$\lim_{\gamma\to 0}\left(\sum_{n=0}^{N} a_n\gamma^n\right)\left(\sum_{n=0}^{N} b_n\gamma^n\right) \approx \sum_{n=0}^{N} d_n\gamma^n.$$

Although these expansions are not easy to express in closed form, they are very suitable for numerical evaluation. At the end, for a non-homogeneous structure the spectrum of the Green's function is approximated in the following form around the branch point

$$\lim_{k_\rho\to k} \tilde{G}(k_\rho) \approx a_0 + a_1\gamma + \sum_{n=2}^{N} a_n\gamma^n. \quad (8)$$

Typical values of the calculated coefficients in (8) are given in Table II.

TABLE II. EXPANSION COEFFICIENTS.

a_0	6.5195012447631873e-002
a_1	-2.1251948240234371e-003
a_2	2.9370518930264711e-005
a_3	3.4341517277598906e-007
a_4	-2.9326239132778149e-008
a_5	7.5078668651253435e-010

A simpler approach to calculate the expansion coefficients (a_n) is based on the application of a numerical fitting algorithm to the cost function (8) with unknown coefficients. This approach can be used to derive only the first 2-3 expansion coefficients with an accuracy sufficient in practice.

For non-homogeneous planar structures, the problematic behavior around the branch-point K can be partially annihilated by subtracting the spectral branch point function:

$$c^K(k_\rho) = \left(\sqrt{k_\rho^2 - K^2} - k_\rho + \frac{K^2}{2\sqrt{k_\rho^2 + K^2}}\right). \quad (9)$$

Its corresponding contribution in space domain is given by:

$$C^K(\rho) = \left(-\left(jK + \frac{1}{\rho}\right)\frac{e^{-jK\rho}}{\rho^2} + \frac{1}{\rho^3} + \frac{K^2}{2}\frac{e^{-K\rho}}{\rho}\right) \quad (10)$$

Then the two counterparts of the annihilated function for the branch point can be written as

$$\tilde{G}_{BP}(k_\rho) = a_1 c^K(k_\rho) \quad (11)$$

$$G_{BP}(\rho) = a_1 C^K(\rho).$$

It should be mentioned that in practice the direct application of formulas (9, 10) can encounter some problems due to numerical loss of significant digits. For instance, it can be shown that for large k_ρ (9) decreases sufficiently fast as $1/k_\rho^3$. However, some terms increase as k_ρ. Although they start to annihilate each other above some spectral distance, numerical annihilation reduces considerably the number of significant digits. The solution consists in the derivation of the asymptotic behavior. Combining the two expansions in (9) One obtains the asymptotic expansion of the annihilating function around the branch point for large k_ρ values

$$\lim_{k_\rho\to\infty} c^K(k_\rho) \approx -\frac{5}{8}\frac{K^4}{k_\rho^3} + \frac{5}{16}\frac{K^6}{k_\rho^5} + \ldots \quad (12)$$

The contribution in spatial domain should have no singularity around ρ=0. However some terms in (10) have a singular behavior ($\frac{1}{\rho^3}$) and can cause numerical problems. The expansion of the exponents in (10) in Taylor series recovers the necessary behavior at the origin

$$\lim_{\rho\to 0} C^K(\rho) \approx -\sum_{n=3}^{N} \frac{(-jK)^n}{n!}\rho^{n-3} - jK\sum_{n=2}^{N}\frac{(-jK)^n}{n!}\rho^{n-2} + \frac{K^2}{2}\sum_{n=1}^{N}\frac{(-K)^n}{n!}\rho^{n-1}. \quad (13)$$

The surface wave poles that have an impact on the evaluation of (1, 3) are located on the k_ρ complex plane close to the real axis. Only for lossless structures these poles are found exactly on the real axis. In any case there are many numerical methods allowing to determine the position of the pole and its residue with prescribed accuracy [7, 8]. Around the pole (P) the spectrum can be approximated

$$\lim_{k_\rho\to P} \tilde{G}(k_\rho) \approx a_{p0} + \frac{a_P}{k_\rho - P} \quad (14)$$

where P is the pole position and a_P is its residue. Any surface wave pole P can be annihilated by subtracting the following spectral function:

$$C^P(k_\rho) = 2P\left(\frac{1}{k_\rho^2 - P^2} - \frac{1}{k_\rho^2 + P^2}\right) = \frac{4P}{k_\rho^4 - P^4}. \quad (15)$$

The corresponding spatial function can be calculated analytically:

$$C^P(\rho) = -\frac{jP}{2}\left(H_0^{(2)}(P\rho) - K_0(P\rho)\right). \quad (16)$$

In contrast to the branch point annihilating function, the calculation of the surface wave annihilating functions encounters no particular numerical problems. The parameters of the poles are indicated in Table III. The total surface wave poles annihilating function is written in the following form for the spectrum in (2)

$$\tilde{G}_P(k_\rho) = \sum_{n=1}^{3} a_{Pn} c^{Pn}(k_\rho) \leftrightarrow G(\rho) = \sum_{n=1}^{3} a_{Pn} C^{Pn}(\rho).$$

TABLE III. PARAMETERS OF SURFACE WAVE POLES.

Pole position, k_ρ / K	Residue, a_P
1.470176488821869	0.115547079056506
1.780369443371680	0.044628852686970
1.947047645135529	0.010392395509118

In this way, the problematic behaviors due to the poles and the branch point are extracted in spectral-domain, leading to a smoother spectral-domain Green's function, which can be efficiently integrated over the interval (0,∞) along the real axis only. The integral is split into two parts due to a different integrand behavior for small and large k_ρ values.

III. NUMERICAL RESULTS

The Green's function calculated using the proposed combined approach agrees very well, as shown in Fig. 2, with the reference solution based on the deformed integration path. As expected the annihilating functions give dominant contributions for large ρ values and small contributions for small ρ values. Future work is focused on the improvement of the annihilating function behavior for the intermediate ρ values by implementing a more complex spectral behavior.

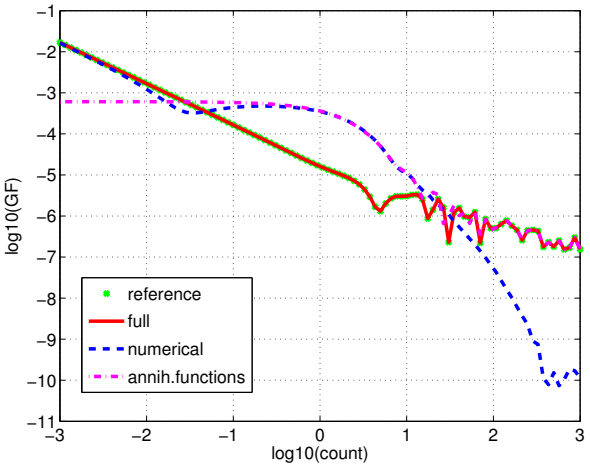

Fig. 2. Numerical Green's function and its different components (ε=4, f=8 GHz, h=3/80 m, ρ=count/k).

REFERENCES

[1] J. R. Mosig, "Arbitrary shaped microstrip structures and their analysis with a mixed potential integral equation," IEEE Trans. Microw. Theory Tech., vol. 36, no. 2, pp. 314–323, 1988.

[2] K. A. Michalski and D. Zheng, "Electromagnetic scattering and radiation by surfaces of arbitrary shape in layered media, Part 1: Theory," IEEE Trans. Antennas Propag., vol. 38, no. 3, pp. 335–344, 1990.

[3] R. Golubovic Niciforovic, A. G. Polimeridis, and Juan R. Mosig, "Fast Computation of Sommerfeld Integral Tails via Direct Integration Based on Double Exponential-Type Quadrature Formulas**",** IEEE Transactions Antennas Propagation, vol. 59, no. 2, pp. 694-699, February 2011

[4] M. Vrancken, G.A.E. Vandenbosch, "Semantics of dyadic and mixed potential field representation for 3D current distributions in planar atified media", IEEE Transactions Antennas Propagation, vol. 51, no. 10, 2778-2787, October 2003

[5] Y. Schols, G.A.E. Vandenbosch, "Separation of horizontal and vertical dependencies in a surface/volume integral equation approach to model quasi 3D structures in multilayered media", IEEE Transactions Antennas Propagation, vol. 55, no. 4, 1086-1094, April 2007

[6] M Vrancken, and GAE Vandenbosch "Hybrid dyadic-mixed-potential and combined spectral-space domain integral-equation analysis of quasi-3-D structures in stratified media", IEEE Trans. Microwave Theory Techniques, vol. 51, no. 1, pp. 216-225, 20

Revision of EBG Metamaterials and Active Antennas

Gonzalo Expósito-Domínguez*‡, José Manuel Fernández-González*, Pablo Padilla†,
Manuel Sierra-Castañer*
*Radiation Group, Signals, Systems and Radiocommunications, Universidad Politécnica de Madrid, 28040, Spain
Email: {gexposito, jmfdez, mscastaner}@gr.ssr.upm.es
†Department of Signal Theory, Telematics and Communications, Universidad de Granada, Granada 18071, Spain.
Email: pablopadilla@ugr.es
‡Department of Antennas and EM Modelling, IMST GmbH, 47475, Germany.

***Abstract*—This review of Electromagnetic Band Gap (EGB) metamaterials and steering integrated antennas was carried out in IMST GmbH under a short collaboration stay. This activity is in line with Coordinating the Antenna Research in Europe (CARE). The aim is to identify the newest trends, and suggest novel solutions and design methodologies for various applications.**

I. Introduction

Starting from the results achieved by the ACE Network of Excellence (from 2004 to 2008), CARE (introduced in 2009), continues and reinforces the collaboration among the European Institutions involved in antenna research. In CARE, the level of cooperation reached in ACE will be sustained and improved by students and researchers secondment, best practices sharing, industrial training and dissemination, by publications and conferences.

This paper gives an overview of the EBG metamaterials theory in section II [1]. The section III is devoted to EBG applications. In section IV the main problems of steering integrated antennas are presented. Finally, in section V the conclusions are drawn.

II. EBG Theory

Electromagnetic Band Gap (EBG) based on Frequency Selective Surfaces (FSS) [2] are one type of metamaterials with electrical properties [3].

EBG technique appears as an application of truncated frequency selective surface (FSS) [4]. These structures consist of an array of metal protrusions on a flat metal sheet and can be visualized as mushrooms protruding from the surface. When the period is small compared to the wavelength of interest, it is possible to analyze the material as an effective medium, with a surface impedance. These "mushrooms" present very high impedance for vertical an horizontal modes at certain frequencies.

These structures can be analyzed as resonant LC circuits, in which the capacitance is provided by the proximity of the metal plates:

$$C = \left[\frac{w\varepsilon_0(\varepsilon_{eff})}{\pi}\right]\cosh^{-1}\left(\frac{2w}{g_0}\right) \tag{1}$$

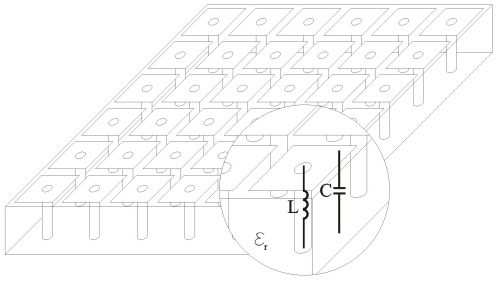

Fig. 1. High impedance surface and its model with parallel resonant LC circuit.

and the inductance is related to the thickness of the structure:

$$L = \mu_0 t \tag{2}$$

Therefore, the surface impedance is given by the following expression:

$$Z_s = \frac{j\omega L}{1-\omega^2 LC} \tag{3}$$

The resonance frequency of the circuit is given by:

$$\omega_0 = \frac{1}{\sqrt{LC}} \tag{4}$$

Below resonance, the surface is inductive meanwhile above resonance, the surface is capacitive. Near ω_0, the surface impedance is much higher than the impedance of free space [4].

III. EBG applications

Among others, EBG structures are used as ground planes emulating Artificial Magnetic Conductors (AMC) in a narrow frequency range. EBG are used also to reduce the mutual coupling between elements.

TABLE I
COMPARISON OF PEC, PMC, AND EBG GROUND PLANES FOR LOW PROFILE ANTENNA DESIGNS.

Ground plane	Reflection phase	Comments
PEC	180°	Reverse image.
PMC	0°	Mutual coupling.
EBG	Varies from 180° to -180° with frequency	Suitable frequency band.

A. EBG Ground plane

EBG structure has one important feature: the in-phase reflection coefficient for plane waves. This property can be used to design low-profile wire antennas [5]. The low-profile design usually refers to the antenna structures whose height is less than one-tenth. In chapter 12 of [6], a comparison between PEC, PMC, and EBG ground planes is carried out. The conclusions are drawn in Table I.

In [7] EBG ground plane is used to reduce the effect of multipath by blocking the propagation of surface waves and cross polarization component in a low profile GALILEO antenna. Its performance is similar to a classical choke ring antenna, but with the advantage of low weight and low profile.

B. Filters

Thanks to its frequency selective feature, this EBG structure can be used as a filter. By applying three elements as a ground plane for a microstrip line, in [8] isolation higher than 55 dB in the first frequency band (2.1 GHz) and 40 dB in the second one (2.45 GHz) are achieved.

C. Mutual coupling reduction

Patch antennas are found to have very strong mutual coupling due to the pronounced surface waves on a thick and high permittivity substrates. However, in order to reduce antenna size and bandwidth enhancement there is no other option. In [9], four columns of EBG patches are inserted between the antennas in a $\epsilon_r = 10.2$ and thickness ($h = 2$ mm) substrate. Finally 8 dB of reduction are obtained. In array applications where the separation between elements is 0.5λ in order to avoid grating lobes, the available space is not enough to introduce four columns of EBG structures. In [10] different substrates are combined, radiating elements are suspended over a thick foam layer in order to increase the bandwith, meanwhile EBG structures are printed in a thin high permittivity substrate for size reduction and surface wave suppression. In [11] by using edge-located vias the size of mushroom-type EBG is reduced by 20%. Among other strategies in [12] a fork shape is used. The area occupied by the fork-like structure is less than 40% of the mushroom-like structure. Besides, Microelectromechanical Systems (MEMS) are used and reconfigurable stop band is obtained.

Another technique studied is metal strips. Basically, the idea is to combine the EBG concept with soft surfaces. A comparison of bandgaps of mushroom-type EBG surface and corrugated and strip-type soft surfaces is shown in [13]. This stripe-type is used in [14] and in [15] to reduce mutual coupling. Finally, dual band planar soft surfaces are developed in [16], two sizes of strips are mixed in order to get dual forbidden band.

New solutions for patch size reduction are proposed. In order to maintain the working frequency with the same substrate thickness, the only parameter available is the capacitance *C*. In order to increase this parameter a multilayered structure is presented in Fig. 2(a) and Fig. 2(b) [17].

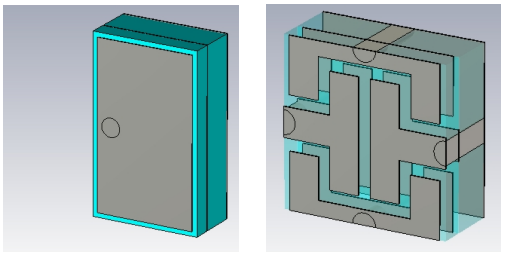

(a) Multilayered patch-shape (b) Multilayered H-shape

Fig. 2. Multilayered mushroom-type solutions.

IV. STEERING APPLICATIONS

The antenna array concept arises due to the necessity of getting higher directivity. By changing the phase feeding of the array elements the radiation pattern can be steered in the desired direction [18] without moving the antenna physically.

A. Active networks

This kind of feeding can be done through active networks such as phase shifters or microelectromechanical systems (MEMS). Those systems have high complexity but high flexibility and features. In [19] MEMS are used in an antenna array front end at 24 GHz. The aim of the project is to combine MEMS with monolithic microwave integrated circuits (MMIC), this system presents low insertion loss, large bandwidth, and good linearity over frequency. In [20] four elements array is fed by coplanar transmission lines (TL). Using MEMS, those TLs change their capacity and propagation velocity, therefore the radiating elements can be fed with the desired phase shift. In [21], a complex system of 156 radiating elements in Ku band is presented. This system is constructed in Low Temperature Co-Fired Ceramic (LTCC) technology, it has linear polarization with tracking, a scan range from 20° to 60° in elevation from horizon and 0° to 360° in azimuth. The antenna size is 20 cm x 20 cm x 2 cm, optimum for car integration. In [22]-[23] the Smart Antenna Terminal (SANTANA) is presented. The system works in Ka-band for reception (RX) and transmission (TX). The uplink frequency is 29.75 GHz and the downlink frequency is 19.95 GHz, this system has the capability of electronic steering in azimuth and elevation and the radiating element is realized in a 16 multilayered LTCC structure. L-band phased array for maritime satcom is shown in [24]. This antenna consists of 26 patch elements that are mounted on a soccer-like spherical

aperture. This design is an innovative and powerful alternative to current mechanically steered systems. The last example, antenna GEODA-GRUA [25] is one conformal adaptative antenna designed for satellite communications. Operating at 1.7 GHz with circular polarization, it is possible to track and communicate with several satellites at once being able to receive signals in full azimuth and within the range of 5º to broadside elevation. The antenna is composed of 2700 radiating elements based on a set of 60 triangular arrays that are divided in 15 subarrays of 3 radiating elements.

B. Passive networks

Another beam control option is passive networks. Butler matrix network [26] consists in 2^n inputs, 2^n outputs, $2^{n-1}\log_2 2^n$ hybrid couplers, crossovers and phase shifters. The function of a Butler matrix is to combine signals in phase going or coming from an antenna array. It produces 2^n beams with constant angular separation. Blass matrix network [27] has two groups of transmission lines which are interconnected through hybrid couplers. The path difference, is the clue in order to control the beam steering. This solutions do not have so good features but are cheaper solutions. In [28] a dual circular polarized steering antenna for satellite communications in X band is presented. This antenna has the following capabilities: broadband capacity (7.25-8.15 GHz) 15%, dual circular polarization (RHCP and LHCP, interchangeable for TX and RX), good axial ratio (AR$<$3dB). Finally this antenna is able to steer in elevation to $45°$, $75°$, $105°$ and $135°$ electronically with a Butler matrix network and $360°$ in azimuth with a motorized junction. In [29], a system based in horn antennas and beamforming networks is shown. This antenna is capable of using several beams simultaneously. On the other hand, solutions based in Traveling Wave Antennas (TWA) [30]-[31], allow to control the direction of the radiation pattern as a function of frequency for a narrow band.

V. Conclusions

During this Short Term Scientific Mission, in IMST under the supervision and guidance of Dr. Marta Martínez-Vázquez a review of metamaterials and active antennas was carried out. The focus of the study was EBG structures and its applications. In future works EBG structures will be applied to reduce mutual coupling between elements in steering applications.

Acknowledgment

This work has been carried out in IMST GmbH, it has been partially funded by the CARE Coordination Action within the FP7 of the European Union (FP7-INFSO-ICT-248272). This thesis is been supported by an UPM grant CH/003/2011, and the SICOMORO project with reference TEC2011-28789-C02-01.

References

[1] P.-S. Kildal. Definition of artificially soft and hard surfaces for electromagnetic waves. *Electronics Letters*, 24(3):168 –170, feb 1988.

[2] D. Sievenpiper, L. Zhang, R. Broas, N. Alexopoulos, and E. Yablonovitch. High-impedance electromagnetic surfaces with a forbidden frequency band. *IEEE Trans. On Microwave Theory and Techniques*, 47:2059–2074, Nov. 1999.

[3] T. Itoh C. Caloz. *Electromagnetic metamaterials: transmission line theory and microwave applications: the engineering approach*. John Wiley and Sons, 2006.

[4] F. Yang and Y. Rahmat-Samii. *Electromagnetic Band Gap Structures in Antenna Engineering*. The Cambridge RF and Microwave Engineering Series, 2008.

[5] Fan Yang and Y. Rahmat-Samii. Reflection phase characterizations of the ebg ground plane for low profile wire antenna applications. *Antennas and Propagation, IEEE Transactions on*, 51(10):2691 – 2703, oct. 2003.

[6] N. Engheta and R. Ziolkowski. *Metamaterials, physics and engineering explorations*. John Wiley and Sons, 2006.

[7] R. Baggen, M. Martinez-Vazquez, J. Leiss, S. Holzwarth, L.S. Drioli, and P. de Maagt. Low profile galileo antenna using ebg technology. *Antennas and Propagation, IEEE Transactions on*, 56(3):667 –674, march 2008.

[8] L. Inclan-Sanchez, J.-L. Vazquez-Roy, and E. Rajo-Iglesias. High isolation proximity coupled multilayer patch antenna for dual-frequency operation. *Antennas and Propagation, IEEE Transactions on*, 56(4):1180 –1183, april 2008.

[9] Fan Yang and Y. Rahmat-Samii. Microstrip antennas integrated with electromagnetic band-gap (ebg) structures: a low mutual coupling design for array applications. *Antennas and Propagation, IEEE Transactions on*, 51(10):2936–2946, Oct. 2003.

[10] E. Rajo-Iglesias, O. Quevedo-Teruel, and L. Inclán-Sánchez. Mutual coupling reduction in patch antenna arrays by using a planar ebg structure and a multilayer dielectric substrate. *IEEE Trans. on Antennas and Propagation*, 56(6):1648–1655, Jun. 2008.

[11] E. Rajo-Iglesias, L. Inclan-Sanchez, J.-L. Vazquez-Roy, and E. Garcia-Muoz. Size reduction of mushroom-type ebg surfaces by using edge-located vias. *Microwave and Wireless Components Letters, IEEE*, 17(9):670 –672, sept. 2007.

[12] Li Yang, Mingyan Fan, Fanglu Chen, Jingzhao She, and Zhenghe Feng. A novel compact electromagnetic-bandgap (ebg) structure and its applications for microwave circuits. *Microwave Theory and Techniques, IEEE Transactions on*, 53(1):183 – 190, jan. 2005.

[13] E. Rajo-Iglesias, M. Caiazzo, L. Inclan-Sanchez, and P.-S. Kildal. Comparison of bandgaps of mushroom-type ebg surface and corrugated and strip-type soft surfaces. *Microwaves, Antennas Propagation, IET*, 1(1):184 –189, february 2007.

[14] E. Rajo-Iglesias, O. Quevedo-Teruel, and L. Inclan-Sanchez. Planar soft surfaces and their application to mutual coupling reduction. *Antennas and Propagation, IEEE Transactions on*, 57(12):3852 –3859, dec. 2009.

[15] O. Quevedo-Teruel, L. Inclan-Sanchez, and E. Rajo-Iglesias. Soft surfaces for reducing mutual coupling between loaded pifa antennas. *Antennas and Wireless Propagation Letters, IEEE*, 9:91 –94, 2010.

[16] E. Rajo-Iglesias, J.-L. Vazquez-Roy, O. Quevedo-Teruel, and L. Inclan-Sanchez. Dual band planar soft surfaces. *Microwaves, Antennas Propagation, IET*, 3(5):742 –748, august 2009.

[17] G. Expósito-Domínguez, P. Padilla-Torre, J. M. Fernández-González, and M. Sierra-Castañer. Mutual coupling reduction techniques in electronic steering antennas in x band. *33^{rd} ESA antenna workshop on challenges for space antenna systems*, Oct. 2011.

[18] C. A. Balanis. *Antenna Theory, analysis and design*. Wiley india, third edition edition, 1997.

[19] M.A. Campo, O. Litschke, T. Vaha-Heikkila, L. Markku, and R. Baggen. Mems-4-mmic: Design of antenna array front end at 24 ghz. In *Antennas and Propagation (EUCAP), Proceedings of the 5th European Conference on*, april 2011.

[20] K. Topalli, O.A. Civi, S. Demir, S. Koc, and T. Akin. A monolithic phased array using 3-bit distributed rf mems phase shifters. *Microwave Theory and Techniques, IEEE Transactions on*, 56(2):270–277, Feb 2008.

[21] R. Baggen, S. Vaccaro, and D.L. del Rio. Design considerations for compact mobile ku-band satellite terminals. In *Antennas and Propagation, 2007. EuCAP 2007. The Second European Conference on*, pages 1 –5, nov. 2007.

[22] A. Stark, A. Dreher, H. Fischer, A. Geise, R. Gieron, M. Heckler, S. Holzwarth, C. Hunscher, A.F. Jacob, K. Kuhlmann, O. Litschke, D. Lohmann, W. Simon, F. Wotzel, and D. Zahn. Santana: Advanced electronically steerable antennas at ka-band. In *Antennas and Propaga-*

tion, 2009. EuCAP 2009. 3rd European Conference on, pages 471 –478, march 2009.

[23] S. Holzwarth, A. F. Jacob, A. Dreher, C. Hunscher, H. Fischer, A. Stark, B. Rohrdantz, A. Geise, K. Kuhlmann, R. Gieron, O. Litschke, D. Lohmann, W. Simon, P. Buchner, M. V. T. Heckler, and L. A. Greda. Active antenna arrays at ka-band: Status and outlook of the santana project. In *Antennas and Propagation (EuCAP), 2010 Proceedings of the Fourth European Conference on*, pages 1 –5, april 2010.

[24] M. Geissler, F. Woetzel, M. Bottcher, S. Korthoff, A. Lauer, M. Eube, and M. Wleklinski. L-band phased array for maritime satcom. In *Phased Array Systems and Technology (ARRAY), 2010 IEEE International Symposium on*, pages 518 –523, oct. 2010.

[25] J.G. Trujillo, M.S. Natera, I. Montesinos, M.A. Campo, M.S. Perez, and R. Martinez. Geoda-grua: Adaptive multibeam conformal antenna for satellites communications. In *General Assembly and Scientific Symposium, 2011 XXXth URSI*, pages 1 –4, aug. 2011.

[26] J. Butler and R. Lowe. Beam-forming matrix simplifies design of electronically scanned antennas. *Electronic Design*, 9:170–173, 1961.

[27] J. Blass. Multi-directional antenna - new approach top stacked beams. *IRE International Convention record*, pages 48–50, 1960.

[28] G. Expósito-Domínguez, P. Padilla-Torre, J. M. Fernández-González, and M. Sierra-Castañer. Dual circular polarized steering antenna for satellite communications in x band. *Progress In Electromagnetic Research*, 122:61–76, 2012.

[29] Morin G. A. Tang M. Q. Richard S. Rao, K.S. and K. K. Chan. Development of a 45 ghz multiple-beam antenna for military satellite communications. *IEEE Transactions on Antennas and Propagation*, 43(10), Oct 1995.

[30] C.H. Walter. *Traveling Wave Antennas*. McGraw-Hill, 1965.

[31] J.N. Hines, V.H. Rumsey, and C.H. Walter. Traveling-wave slot antennas. *Proceedings of the IRE*, 41(11):1624–1631, Nov 1953.

Thermal Calculation Using a 3D-EM Solver and Thermal-Electrical Analogy

Ismael Nistal-González[1,2], Andreas Bettray[1], Kai Maulwurf[1]

[1]Dept. of Antennas & EM Modelling
IMST GmbH
Kamp-Lintfort, Germany
nistal@imst.de

[2] Dept. of Signal Theory and Communications
Universidad Carlos III de Madrid
Leganés, Spain

Abstract—**In this paper, a steady state thermal simulation approach is implemented, which makes use of a conventional electromagnetic simulator in order to take advantage of the existing software. To solve the problem, the thermal-electrical analogy will be taken into account, including conduction, convection and radiation. Empire XCcel™ along with a script implemented in Python have been used to simulate the built prototypes. The validation of the proposed method has been carried out with an infra-red camera.**

Thermal simulation; conduction; convection; radiation; thermal-electrical analogy; EM simulation

I. INTRODUCTION

Nowadays, due to highly integrated packaging and high power used in electronic designs, thermal analysis is a crucial aspect, which aims at predicting the working temperature of a device. This analysis can be performed using various software tools and Computational Fluid Dynamics (CFD) simulators. Yet, these are not always available for RF designers, and moreover the complexity of the system may require long simulation times. Online tools are also available to generate simple thermal simulations in the steady state [1] or it can be done manually by an equivalent circuit model [2]. In most cases, these two approaches do not fulfill all the requirements or the precision is not good enough.

The model presented here can be easily implemented into existing electromagnetic simulation software with acceptable levels of simulation time. The thermal-electrical analogy was used in order to evaluate the 3D heat distribution of an electronic device. The main mechanisms of heat transfer, namely conduction, convection and radiation, were integrated in the model. Empire XCcel™ [3] was used for the simulations. This is a versatile and powerful 3D-EM solver based on the FDTD method. The simulation results and the accuracy of the method were validated by measuring a set of PCBs using an infra-red (IR) camera.

II. THERMAL-ELECTRICAL ANALOGY

Due to the similarity between thermal and electrical conduction, it is possible to perform thermal analysis using an EM solver. Indeed, Poisson´s equation for electrical charge can be assimilated to the heat-equation in the steady state [4] by using the following transformations shown in Table I.

TABLE I. THERMAL-ELECTRICAL ANALOGY CONVERSION TABLE.

Electrical	Thermal
Voltage (V)	Temperature (K)
Current (A)	Power (W)
Electrical Conductivity ($\Omega^{-1}m^{-1}$)	Thermal Conductivity (W/(mK))
Electrical Resistance (Ω)	Thermal Resistance (K/W)

III. METHOD

Using the proposed analogy, the 3D-EM solver has to be initialized with the following requirements:

1) The electrical conductivity of the materials has to contain its specific thermal conductivity.
2) Special components such as coolers or chip packages are simulated as electrical resistances with the thermal resistance value provided by the manufacturer. If the heat is dissipated over an area (e.g. convection, radiation and even heat sinks), it is used a *sheet resistor* in Empire. This resistance is defined in an area.
3) Thermal power sources are modelled using electrical current sources.
4) DC simulation is used to get the thermal solution in the steady state.

It is common practice to perform a simple thermal analysis once the thermal characteristics of the components to be used are known. For example, using the thermal conductivity of the materials, the junction-to-case thermal resistance of the chip (ability to dissipate heat from the surface of the die to the outside surface of the package), the heatsink-to-ambient thermal resistance if necessary (which includes convection and radiation as well), and neglecting natural convection and radiation elsewhere, it is possible to predict the temperature and even the heat distribution using the proposed solution. Actually, when the convection (and radiation) heat transfer coefficient h (W/(m^{2}K)) is known, it is also possible to take it into account over the structure, and simulate it as a resistance in a determined area.

The problem arises when this information is not available. The model proposed here is capable of predicting the

temperature and heat distribution in a 3D structure under these unfavorable conditions. The main difficulty appears when calculating convection and radiation, because of their dependence on the surface temperature, which is in fact the unknown variable. A set of functions programmed in Python [5] allows executing the required simulations iteratively with Empire. These functions include the calculation of the heat dissipated by radiation and convection [6]-[7] as exposed below:

$$q_T = q_{conv} + q_{rad} = hA(T_s - T_\infty) + \varepsilon A\sigma(T_s^4 - T_{surr}^4) \quad (1)$$

$$h = \begin{cases} \frac{k}{L} 0.54 Ra_L^{1/4}, & 10^4 \le Ra_L \le 10^7 \\ \frac{k}{L} 0.15 Ra_L^{1/3}, & 10^7 < Ra_L \le 10^{11} \end{cases} \quad (2)$$

$$Ra_L = \frac{g\beta\mu C(T_S - T_\infty)L^3}{\nu^2 k}, L = \frac{A}{P} \quad (3)$$

where q_T is the power dissipated by convection and radiation (W), A is the area exposed to the air (m^2), h is the convection heat transfer coefficient ($W/(m^2K)$), T_s is the surface temperature of the probe (K), T_∞ (=T_{surr}) is the air temperature (K), ε is the emissivity of the surface, σ is the Stefan-Boltzmann constant ($5.67 \cdot 10^{-8}$ $W/(m^2K^4)$), k is the thermal conductivity of the air (W/(mK)), L is the characteristic length (m), Ra is the Rayleigh number (dimensionless), g is the gravitational acceleration (m/s^2), β is the volumetric thermal expansion coefficient (K^{-1}), μ is the dynamic viscosity (kg/(ms)), C is the specific heat capacity (J/(kgK)), ν is the kinematics viscosity (m^2/s) and P is the perimeter of the probe (m).

With this method the temperature on the area exposed to the air is evaluated so that it is possible to calculate the convection and radiation in the steady state. Since the temperature is not known in the beginning, two arbitrary initial coefficients are used. These values do not affect the final result. After the first iteration of the simulation, the temperature in the 3D structure is accessible, and the coefficients derived from it are used for the new iteration. The routine simulates the structure and calculates the coefficients until convergence in the temperature of the structure is obtained. One of the main challenges was the calculation of the surface temperature: averaging the temperature in the entire non-isothermal surface could lead to erroneous results if, for example, the heat source is too small compared to the complete surface. The method which offered better results consists in dividing the surface into different regions where the temperature is almost constant. Afterwards, convection and radiation are calculated in each region.

In this methodology heat sinks can also be included when natural convection is not the main cooling mechanism. Usually, heatsink-to-ambient thermal resistance is provided by the manufacturer, which is strongly dependent on the power used to calculate it. The more power, the more temperature difference between the heat sink and the ambient, which implies more heat dissipated by convection and radiation, and therefore better heat sink performance (lower thermal resistance value). So, if an accurate analysis is required, it is necessary either use the same power in the device as the manufacturer or evaluate analytically convection and radiation in the heat sink [8]-[10].

IV. Comparison between Simulation and Measurements

As stated above, a set of PCBs has been fabricated to compare simulation and measurement results. The proposed PCBs are made of Rogers RO4350B material, with Surface Mount Devices (SMD) resistors as heat sources. All PCBs include two main sources with 8 SMD resistors each. Both sources are connected through a copper line, and 5 measurement points are defined between the two sources. From PCB1 to PCB3 the only difference is the width of the copper line (2, 4 and 8 mm). PCB4-6 are all the same than PCB2 (4 mm line) but with a ground plane, solder mask all over the surface, and ground plane plus 4 vias in the copper line between the first measurement point and the source, respectively.

The measurements were made with an IR camera FLIR T335 to prevent intrusion on measurements. Besides, it also gives the possibility to check the heat distribution with Empire. An anti-glare-spray was used to cover the surface to compensate the differences in the emissivity of the materials used in the PCBs. Its emissivity was calculated by using an aluminum plate (HT-306) covered by the anti-glare-spray and including a thermocouple (Multimeter Fluke 289) on it. The aluminum plate was heated up from 28 to 140 °C, and the emissivity parameter of the camera was modified to have the same temperature in both, the thermocouple and the camera. Considering the same temperature all over the plate, the value obtained was 0.93. Under the PCBs, a piece of foam with very low thermal conductivity was settled in order to avoid the heat dissipation and to maintain the free air convection as the main cooling mechanism.

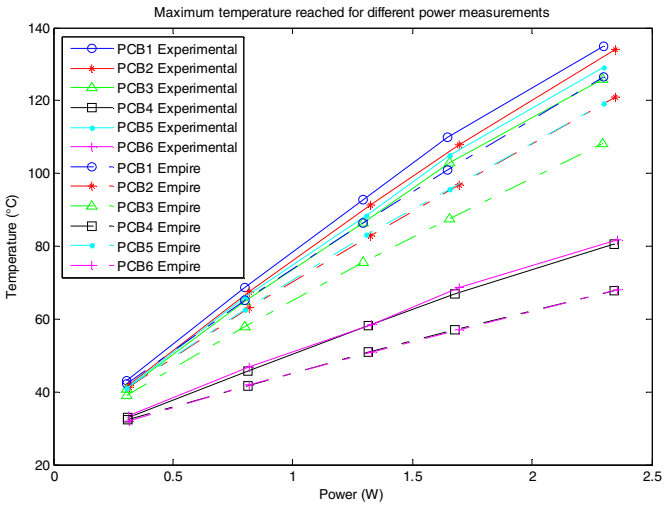

Figure 1. Maximum temperature reached in the surface of the PCB for different power excitations.

The prototypes were measured using different power excitations as shown in Fig. 1. The relative temperature values predicted by Empire between the PCBs are very close to the experimental ones, showing a huge effect if a ground plane is

settled below the structure. Empires offers also a good estimation when using vias (PCB6). It demonstrates, in comparison with the prototype without them (PCB4), that their effect on temperature is almost imperceptible. It could be due to the small thickness of the substrate, which avoids having a direct path between the sources and the ground plane to dissipate heating. On the other hand, the maximum temperature values are lower than the ones obtained in the measurements. This error may come from the approximation method used to calculate the temperature average, which could increase the surface temperature estimated and, consequently, the heat dissipated by convection and radiation. Also, the thermal conductivity of the materials was not checked experimentally and it may vary. As additional information, Fig. 2 offers the temperature obtained in each measurement point. Both, the experimental and the simulated results, show a very good agreement with similar shaped curves and values.

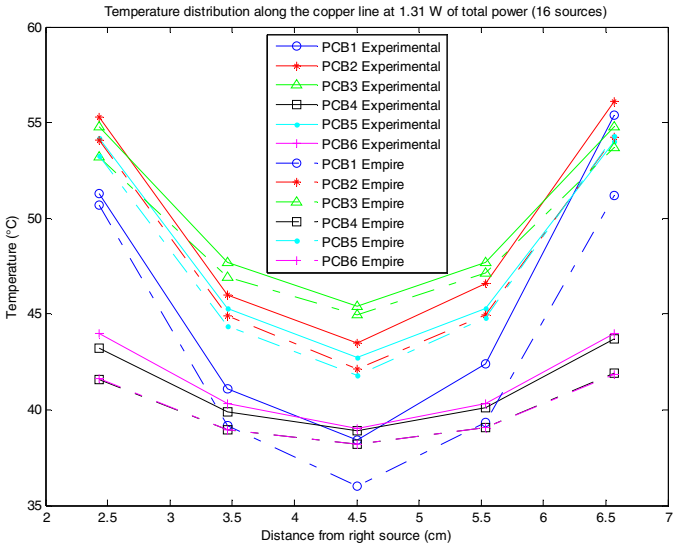

Figure 2. Temperature distribution along the copper line for both, the IR camera and Empire.

Finally, the heat distribution will be also plotted in Fig. 3 and Fig. 4, showing close behavior. In case the ground plane is present (Fig. 4), it can be visualized how the heat spreads because of its high thermal conductivity, hence reducing the maximum temperature.

The simulation time was about 12 minutes per PCB. In case of the PCB4 showed in Fig. 4, the program converged after 4 iterations. Each iteration lasted 3 minutes with a memory consumption of 400 Mbytes in a 2.13 GHz dual core computer.

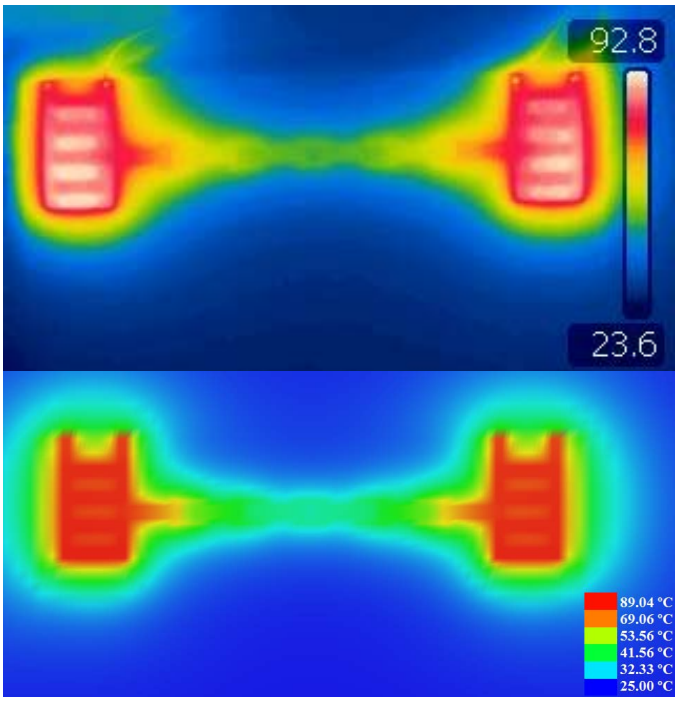

Figure 3. Heat distribution on the PCB1 at 1.3W. Measurement with an IR Camera (*top*). Simulation with Empire (*bottom*).

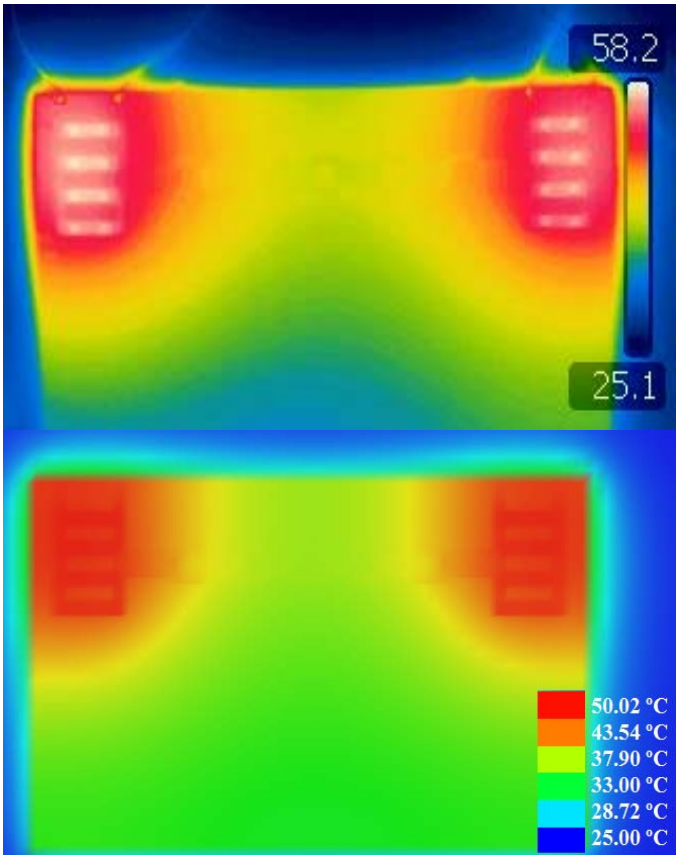

Figure 4. Heat distribution on the PCB4 at 1.3W. Measurement with an IR Camera (*top*). Simulation with Empire (*bottom*).

V. CONCLUSIONS

A thermal analysis has been proposed using an EM solver through the thermal-electrical analogy. Both, convection and radiation have been included in the method programmed in Python. The calculation, implementation and validation of the temperature average methods, was one of the most time costly tasks in the project.

The methodology proposed is also very flexible to different circumstances. That is to say, changing the convection heat transfer coefficient is possible to test different probe positions (inclined, vertical or horizontal), fluids (air, water), environments (internal or external flow), and conditions (free or forced convection).

Using a *sheet resistor* in Empire (for heat sink, convection or radiation), a better approximation of the heat distribution was offered, since the heat is dissipated in an area and not in a fixed point.

Finally, a set of PCBs were built, measured and compared with the Empire results, showing a very good agreement in the temperature estimated.

ACKNOWLEDGMENT

This work has been partially funded by the CARE Coordination Action within the FP7 of the European Union (FP7-INFSO-ICT-248272).

REFERENCES

[1] Thermal Design of Electronics, Frigus Primore, http://frigprim.x10.mx/.

[2] A. Jain, R. E. Jones, R. Chatterjee, and S. Pozder, "Analytical and Numerical Modeling of the Thermal Performance of Three-Dimensional Integrated Circuits," IEEE Trans. Components and Packaging Technologies, vol. 33, pp. 56-63, Mar. 2010.

[3] EMPIRE XCcel Reference Manual, http://www.empire.de/.

[4] L. Jiang, S. Kolluri, B. J. Rubin, H. Smith, E. G. Colgan, M. R. Scheuermann, J. A. Wakil, A. Deutsch, and J. Gill, "Thermal Modeling of On-Chip Interconnects and 3D Packaging Using EM Tools," IEEE Electrical Performance of Electronic Packaging, pp. 279-282, Oct. 2008.

[5] Python documentation, http://python.org/doc/.

[6] F . P. Incropera, D. P. Dewitt, T. L. Bergman, and A. S. Lavine, Fundamental of Heat and Mass Transfer, 6th ed. New York: Wiley, 2007.

[7] J. H. Lienhard IV, and J. H. Lienhard V, A Heat Transfer Textbook, 4th ed. Massachussets: Phlogiston Press, 2011, pp. 399-457, 527-596.

[8] A. D. Kraus, and A. Bar-Cohen, Design and Analysis of Heat Sinks. New York: Wiley, 1995.

[9] Y. Shabany, "Radiation Heat Transfer from Plate-Fin Heat Sinks," IEEE Semiconductor Thermal Measurement and Management Symposium, pp. 132-136, Mar. 2008.

[10] P. Teertstra, M. M. Yovanovich, and J. R. Culham, "Analytical Forced Convection Modeling of Plate Fin Heat Sinks," IEEE Semiconductor Thermal Measurement and Management Symposium, pp. 34-41, Mar. 1999.

Time-Domain Surface Impedance of a Plasmonic Half-Space

Martin Štumpf
Department of Radio Electronics (DREL)
Brno University of Technology
Purkynova 118, 612 00 Brno, the Czech Republic
Email: martin.stumpf@centrum.cz

Guy A. E. Vandenbosch
Electrical Engineering Department (ESAT)
TELEcommunications & MICrowaves
Katholieke Universiteit Leuven
Kasteelpark Arenberg 10 bus 2444
B-3001 Heverlee (Leuven), Belgium
Email: guy.vandenbosch@esat.kuleveu.be

***Abstract*—In this paper we report a part of the results of the research that has been carried out thanks to the financial support of the EU-FP7 CARE (Coordinating the Antenna Research in Europe) Project. As a result of the established cooperation between BUT (Brno University of Technology, the Czech Republic) and K.U.Leuven (Katholieke Universiteit Leuven, Belgium) we present the time-domain surface impedance connected with a plane-wave incidence on a half-space with plasmonic properties. It is shown that by a simple choice of branch-cuts the time-domain surface impedance can be expressed via a definite one-dimensional integral of elementary functions only. Illustrative numerical examples are presented.**

I. Introduction

Ever increasing interest in the time-domain modeling of dispersive materials [1], electromagnetic artificial media [2] and conducting materials at optical frequencies [3, Sec. 3-12] has invoked a need of understanding to the basic problems involved. The reflection and refraction of plane waves at planar interfaces can be included in this category. The corresponding frequency-domain solution is well known for dielectric as well as for conducting media [4, Sec. 9]. On the other hand, the time-domain solution for the latter is a subject seldom touched upon. In this respect, a transient plane wave incident on a conducting half-space and its time-domain surface impedance has been investigated in [5], [6] and [7], respectively. Here, the exact time-domain surface impedance is expressed using the Lipschitz-Hankel integrals [8].

Applications of these results can be primarly found in the time-domain finite-difference modeling [9], where the approximate time-domain surface impedance conditions associated with a plane-wave incidence on a half-space with conducting and dielectric properties have been implemented. Although a uniqueness proof requires boundary conditions that express the local proportionality of the tangential electric and magnetic fields without any other parameters of the relevant wave motion, the surface impedances depending on the angle of incidence of a plane wave have been previously applied to a number of practical problems [10].

In this paper we describe the approach for a computation of time-domain surface impedances associated with an oblique plane-wave incidence on a half-space with plasmonic properties. Our method brings closed-form expressions containing elementary functions only. They are, to the authors' knowledge, in their present form new. Moreover, our expressions can be readily evaluated numerically within any prescribed precision and therefore they are exact. Although we for simplicity consider the Drude model only, the presented technique can be easily extended for any Boltzmann-type relaxation behavior as Lorentz-line or Debye-absorption. Numerical examples are presented.

II. Problem description

The configuration under consideration is given in Fig. 1. In it, the position is specified by the orthogonal Cartesian coordinates $\{x_1, x_2, x_3\}$ with respect to an orthogonal Cartesian reference frame with the origin O and three mutually perpendicular base vectors $\{\boldsymbol{i}_1, \boldsymbol{i}_2, \boldsymbol{i}_3\}$ of unit length each. The time coordinate is t. The configuration consists of half-

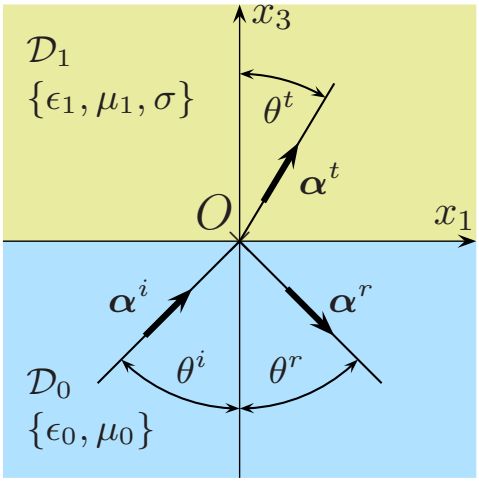

Fig. 1. Problem configuration.

space $\mathcal{D}_0 = \{-\infty < x_1 < \infty, -\infty < x_2 < \infty, -\infty < x_3 < 0\}$ described by its scalar, real and positive electric permittivity ϵ_0 and magnetic permeability μ_0 and of half-space $\mathcal{D}_1 = \{-\infty < x_1 < \infty, -\infty < x_2 < \infty, 0 < x_3 < \infty\}$ described by its scalar, real and positive electric permittivity ϵ_1, magnetic permeability μ_1. Considering the Drude model

[11], the plasmonic properties are accounted for via the electric conduction relaxation function

$$\sigma(t) = \sigma_C \nu_C \exp(-\nu_C t) H(t) \tag{1}$$

with the corresponding dispersive complex-frequency domain equivalent

$$\hat{\sigma}(s) = \sigma_C \nu_C / (s + \nu_C) \tag{2}$$

where $\sigma_C = n_e e^2 / m_e \nu_C > 0$ is connected with the electron plasma angular frequency $\omega_{pe} = (n_e e^2/\epsilon_0 m_e)^{1/2} > 0$, ν_C is the collision frequency, e is the electron charge, n_e is the electron density and m_e denotes the effective electron mass.

The E- or H-polarized electromagnetic plane wave hits the plasmonic half-space with the incident angle θ^i or propagation vector $\boldsymbol{\alpha}^i$. Upon enforcing the boundary conditions across the interface, the reflected and transmitted plane-waves with $\{\theta^r, \theta^t\}$ or $\{\boldsymbol{\alpha}^r, \boldsymbol{\alpha}^t\}$ can be determined, respectively. In view of the problem configuration, the electromagnetic field decomposes into E-polarized and H-polarized subsets with the electric and magnetic field parallel to the interface, respectively. The surface impedances are computed for these subsets separately and read the following forms [7]

$$\hat{Z}_E(s) = \left(\frac{\mu_1}{\epsilon_1}\right)^{1/2} \left[\frac{\hat{\sigma}(s)}{s\epsilon_1} + \cos^2(\tilde{\theta}^t)\right]^{-1/2} \tag{3}$$

for E-polarized fields and

$$\hat{Z}_H(s) = \frac{(\mu_1/\epsilon_1)^{1/2}}{1 + \hat{\sigma}(s)/s\epsilon_1} \left[\frac{\hat{\sigma}(s)}{s\epsilon_1} + \cos^2(\tilde{\theta}^t)\right]^{1/2} \tag{4}$$

for H-polarized fields. Here, $\tilde{\theta}^t$ denotes the"lossless refraction angle"

$$\sin(\tilde{\theta}^t) = (\epsilon_0 \mu_0 / \epsilon_1 \mu_1)^{1/2} \sin(\theta^i) \tag{5}$$

that can be found from Snell's law.

III. Problem solution

Here we derive the expressions for the time-domain surface impedances associated with an oblique E- and H-polarized plane-wave incidence on the plasmonic half-space.

A. E-polarization

Substitution of Eq. (2) into Eq. (3) gives

$$\hat{Z}_E(s) = (\mu_1/\epsilon_1)^{1/2} \hat{F}_E(s) / \cos(\tilde{\theta}^t) \tag{6}$$

with

$$\hat{F}_E(s) = \frac{[s(s+\nu_C)]^{1/2}}{[s(s+\nu_C) + \alpha\nu_C]^{1/2}} \tag{7}$$

where $\alpha = \sigma_C/\epsilon_1 \cos^2(\tilde{\theta}^t)$. The time-domain surface impedance is found via direct evaluation of the Bromwich integral with the help of basic complex number theory. In this case, the integrand contains four branch-points at $s = \{0, -\nu_C, s_B, s_B^*\}$ that are associated with the square-root expressions and $s_B = -\nu_C/2 + \mathrm{i}\Omega$ with $\Omega = (\nu_C/2)(4\alpha/\nu_C - 1)^{1/2} > 0$ assuming $\alpha \geq \nu_C/4$. The horizontal branch-cuts are chosen such that $\mathrm{Re}(s^{1/2}) > 0$ and $\mathrm{Re}[(s+\alpha)^{1/2}] > 0$, i.e. the corresponding polar angles are restricted to the interval $(-\pi, \pi)$ and for $[s(s+\nu_C)+\alpha]^{1/2}$ we restrict the corresponding polar angles to $(-\pi/2, 3\pi/2)$. For the expression to be integrated we get two finite branch-cuts crossing each other $\{s \in \mathcal{C}, -\nu_C < s < 0, s_B < s < s_B^*\}$. In virtue of Cauchy's theorem and Jordan's lemma the Bromwich contour $\mathcal{B}$ is replaced by a finite loop around the branch-cuts and we after a few steps arrive at

$$\begin{aligned} F_E(t) - \delta(t) = \\ -\frac{1}{\pi}\frac{\nu_C}{2}\exp(-\nu_C t/2)\left[\int_{\psi=0}^{\pi/2} F(\psi)\mathrm{d}\psi - \int_{\psi=\pi/2}^{\pi} F(\psi)\mathrm{d}\psi\right] \\ +\frac{1}{\pi\mathrm{i}}\frac{\nu_C}{2}\exp(-\nu_C t/2)\left[\int_{\chi=0}^{\pi/2} G(\chi)\mathrm{d}\chi - \int_{\chi=\pi/2}^{\pi} G(\chi)\mathrm{d}\chi\right] \end{aligned} \tag{8}$$

with

$$F(\psi) = \frac{\sin^2(\psi)}{[4\alpha/\nu_C - \sin^2(\psi)]^{1/2}} \exp[\nu_C t \cos(\psi)/2] \tag{9}$$

$$G(\chi) = [4\alpha\cos^2(\chi)/\nu_C + \sin^2(\chi)]^{1/2} \exp[-\mathrm{i}\Omega t \cos(\chi)] \tag{10}$$

keeping $[\cdots]^{1/2} > 0$. Eq. (8) can be further simplified using $\sinh(x)$ and $\sin(x)$, but this form seems to be convenient for a numerical implementation. In view of Eq. (6) the desired expression for the time-domain surface impedance can be written as

$$Z_E(t) = (\mu_1/\epsilon_1)^{1/2} F_E(t) / \cos(\tilde{\theta}^t) \tag{11}$$

Eq. (11) can be readily evaluated numerically within any prescribed accurracy.

B. H-polarization

Substitution of Eq. (2) into Eq. (4) gives

$$\hat{Z}_H(s) = (\mu_1/\epsilon_1)^{1/2} \hat{F}_H(s) \cos(\tilde{\theta}^t) \tag{12}$$

with

$$\hat{F}_H(s) = \frac{[s(s+\nu_C)]^{1/2}}{s(s+\nu_C) + \beta\nu_C} [s(s+\nu_C) + \alpha\nu_C]^{1/2} \tag{13}$$

where $\alpha = \sigma_C/\epsilon_1 \cos^2(\tilde{\theta}^t)$ and $\beta = \sigma_C/\epsilon_1$. Again, the time-domain surface impedance is found via direct evaluation of the Bromwich integral with the help of basic complex number theory. In this case, the integrand contains four branch-points at $s = \{0, -\nu_C, s_B, s_B^*\}$ that are associated with the square-root expressions, where $s_B = -\nu_C/2 + \mathrm{i}\Omega$ with $\Omega = (\nu_C/2)(4\alpha/\nu_C - 1)^{1/2} > 0$ and two simple pole singularities at $s = \{s_P, s_P^*\}$, where $s_P = -\nu_C/2 + \mathrm{i}\Gamma$ with $\Gamma = (\nu_C/2)(4\beta/\nu_C - 1)^{1/2} > 0$ assuming $\beta \geq \nu_C/4$. The horizontal branch-cuts are chosen such that $\mathrm{Re}(s^{1/2}) > 0$ and $\mathrm{Re}[(s+\alpha)^{1/2}] > 0$, i.e. the corresponding polar angles are restricted to the interval $(-\pi, \pi)$ and for $[s(s+\nu_C)+\alpha]^{1/2}$ we restrict the corresponding polar angles to $(-\pi/2, 3\pi/2)$. For

the expression to be integrated we get two finite branch-cuts crossing each other $\{s \in \mathcal{C}, -\nu_C < s < 0, s_B < s < s_B^*\}$. In virtue of Cauchy's theorem and Jordan's lemma the Bromwich contour $\mathcal{B}$ is replaced by a finite loop around the branch-cuts and simple poles. After a few steps we arrive at

$$F_H(t) - \delta(t) = -\frac{1}{\pi}\frac{\nu_C}{2}\exp(-\nu_C t/2) \times \left[\int_{\psi=0}^{\pi/2} F(\psi)\mathrm{d}\psi - \int_{\psi=\pi/2}^{\pi} F(\psi)\mathrm{d}\psi\right] + \frac{1}{\pi \mathrm{i}}\frac{\nu_C}{2}\left(\frac{4\alpha}{\nu_C} - 1\right)\exp(-\nu_C t/2) \times \left[\int_{\chi=0}^{\pi/2} G(\chi)\mathrm{d}\chi - \int_{\chi=\pi/2}^{\pi} G(\chi)\mathrm{d}\chi\right] \quad (14)$$

with

$$F(\psi) = \frac{[4\alpha/\nu_C - \sin^2(\psi)]^{1/2}}{4\beta/\nu_C - \sin^2(\psi)}\sin^2(\psi)\exp[\nu_C t\cos(\psi)/2] \quad (15)$$

$$G(\chi) = \frac{N(\chi)}{D(\chi)} = \frac{[4\alpha\cos^2(\chi)/\nu_C + \sin^2(\chi)]^{1/2}}{4\beta/\nu_C - 4\alpha\cos^2(\chi)/\nu_C - \sin^2(\chi)} \times \sin^2(\chi)\exp[-\mathrm{i}\Omega t\cos(\chi)] \quad (16)$$

keeping $[\cdots]^{1/2} > 0$. Eq. (14) can be further simplified using $\sinh(x)$ and $\sin(x)$, but this form seems to be convenient for a numerical implementation. The integrals along the vertical branch-cut are unbounded at $\chi_{P1,2} = \cos^{-1}(\pm\Gamma/\Omega)$ and have to be evaluated in the sense of Cauchy principal value. Upon extracting the simple pole singularities we end up with

$$\mathrm{P.V.}\, F_H(t) - \delta(t) = -\frac{1}{\pi}\frac{\nu_C}{2}\exp(-\nu_C t/2) \times \left[\int_{\psi=0}^{\pi/2} F(\psi)\mathrm{d}\psi - \int_{\psi=\pi/2}^{\pi} F(\psi)\mathrm{d}\psi\right] + \frac{1}{\pi \mathrm{i}}\frac{\nu_C}{2}\left(\frac{4\alpha}{\nu_C} - 1\right)\exp(-\nu_C t/2) \times \left[\int_{\chi=0}^{\pi/2} \frac{N(\chi) - N(\chi_{P1})}{D(\chi)}\mathrm{d}\chi - \int_{\chi=\pi/2}^{\pi} \frac{N(\chi) - N(\chi_{P2})}{D(\chi)}\mathrm{d}\chi\right] \quad (17)$$

In view of Eq. (12) the desired expression for the surface impedance can be written as

$$Z_H(t) = (\mu_1/\epsilon_1)^{1/2}\mathrm{P.V.}\, F_H(t)\cos(\tilde{\theta}^t) \quad (18)$$

that is bounded in the integration interval and can be evaluated numerically.

IV. Discussion of Results

This section focuses on a parametric analysis of the time-domain surface impedances of the plasmonic half-spaces. Parameters in our numerical examples are the relative electric permittivity ϵ_1/ϵ_0, relative magnetic permeability μ_1/μ_0, relative parameter $\beta/\nu_C = \sigma_C/\nu_C\epsilon_1$ and the incidence angle θ^i. Two important cases shall are considered: A) high relative electric permittivity $\epsilon_1/\epsilon_0 >> 1$ or/and high relative magnetic permeability $\mu_1/\mu_0 >> 1$ or/and incidence angles approaching to the normal incidence, $\tilde{\theta}^i = 0$. For this case, the corresponding lossless refraction angle approaches to zero and the surface impedances for E- and H-polarized fields are equal in limit; B) relative permitivity and permeability of $\mathcal{D}_1$ that approach to one $\epsilon_1/\epsilon_0 = \mu_1/\mu_0 \downarrow 1$ with small grazing angle. The normalized time-domain surface impedances

$$Z_{E,H;\mathrm{norm}}(t) = 2(\epsilon_1/\mu_1)^{1/2} Z_{E,H}(t)/\nu_C \quad (19)$$

are observed within the time-window $\{10^{-3} \le \nu_C t \le 10^2\}$ having normalized time $t_{\mathrm{norm}} = \nu_C t$. The input parameters are included in the lossless refraction angle $\tilde{\theta}^t$ with β/ν_C.

Figs. 2 and 3 show the time-domain surface impedances for E- and H-polarized fields for two values of the lossless refraction angle $\tilde{\theta}^t = \{18.747°, 69.881°\}$ with $\beta/\nu_C = 2.0$.

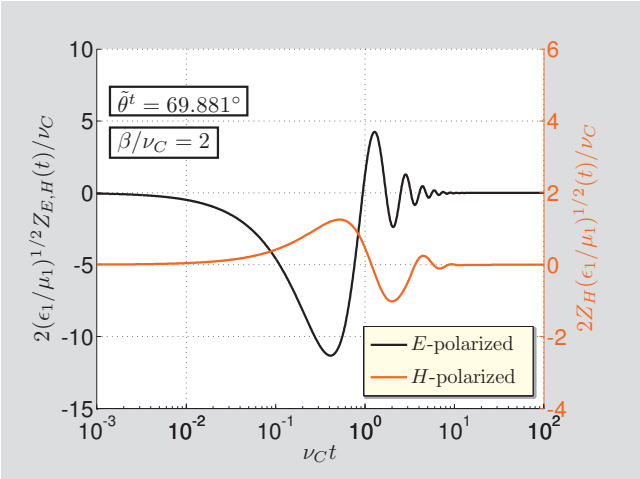

Fig. 2. Normalized E- and H-polarized surface impedances of the plasmonic half-space with respect to the normalized time with $\tilde{\theta}^t = 18.747°$.

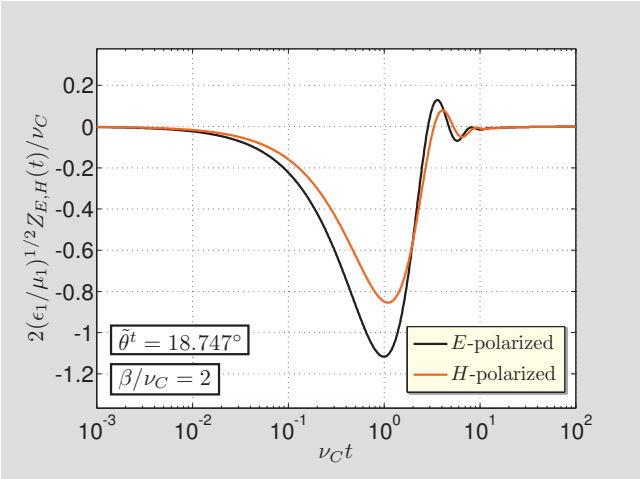

Fig. 3. Normalized E- and H-polarized surface impedances of the plasmonic half-space with respect to the normalized time with $\tilde{\theta}^t = 69.881°$.

The first value corresponds, for example, to $\epsilon_1/\epsilon_0 = 4.0$, $\mu_1/\mu_0 = 1.0$ and $\theta^i = 40^\circ$ while the second value can be found from $\epsilon_1/\epsilon_0 = 1.1$, $\mu_1/\mu_0 = 1.0$ and $\theta^i = 80^\circ$. The surface impedances for the lower lossless refraction angle approach to each other. However, in contrast to the surface impedances of the conducting half-space [7], the surface impedances of the plasmonic half-space do not start at a non-zero constant value but at zero, linearly in time. Next, E-polarized surface impedance always begins with a negative slope that depends on parameters of the plasmonic half-space as well as on the incident angle. On the other hand, the starting slope of the H-polarized surface impedance can be either positive or negative depending on the relative electric permittivity and relative magnetic permeability of $\mathcal{D}_1$ in relation to the incident angle (compare Fig. 2 with 3). Making use the theorem of Abel for one-sided Laplace transformation, we can find that both surface impedances tend to zero as time grows to infinity, i.e. $Z_{E,H}(t) = 0$ as $t \to \infty$. Note that the incident angle for which $\alpha = 2\beta$ for $\epsilon_1/\epsilon_0 = 1.1$ and $\mu_1/\mu_0 = 1.0$ is $\theta^i|_{\alpha=2\beta} = \sin^{-1}(\sqrt{0.55}) \approx 47.87^\circ$, which explains the positive slope $\mathrm{d}Z_{H;\mathrm{norm}}/\mathrm{d}t > 0$ at early time in Fig. 2 for $\theta^i = 80.0^\circ$. For the normal incidence $\theta^i = 0$, the simple pole singularities $\{s_P, s_P^*\}$ are equal to the branch-points $\{s_B, s_B^*\}$, respectively and Eqs. (11) and (18) give the same results.

V. Conclusion

In this paper we have derived simple expressions describing the time-domain surface impedances associated with an oblique plane-wave incidence on the plasmonic half-space. The expressions contain just elementary functions and can be easily evaluated numerically within any prescribed precision. Given numerical examples with the brief discussion on an early- and late-time behavior illustrate the influence of input configurational parameters.

Acknowledgment

The results described in this paper and the research leading to these results have been financed by the EU-FP7 CARE (Coordinating the Antenna Research in Europe) Project (Grant no. 248272). This support is gratefully acknowledged.

References

[1] J.L. Young and R.O. Nelson, "A summary and systematic analysis of FDTD algorithms for linearly dispersive media," *IEEE Antennas Propagat. Mag.*, vol. 43, no. 1, pp. 61–77, Feb. 2001.

[2] R.W. Ziolkowski, E. Heyman, "Wave propagation in media having negative permittivity and permeability," *Physical Revew E*, vol. 64, no. 5, p. 056625, Nov. 2001.

[3] A. Ishimaru, *Electromagnetic Wave Propagation, Radiation and Scattering*, Englewood Cliffs, NJ: Prentice Hall, 1991.

[4] J. A. Stratton, *Electromagnetic Theory*, New York, NY: McGraw-Hill, 1991.

[5] H.Y. Pao, S.L. Dvorak and D.G. Dudley, "An accurate and efficient analysis for transient plane waves obliquely incident on a conductive half space (TE case)," *IEEE Trans. Antennas Propag.*, vol. 44, no. 7, pp. 918–924, Jul. 1996.

[6] H.Y. Pao, S.L. Dvorak and D.G. Dudley, "An accurate and efficient analysis for transient plane waves obliquely incident on a conductive half space (TE case)," *IEEE Trans. Antennas Propag.*, vol. 44, no. 7, pp. 925–932, Jul. 1996.

[7] H.Y. Pao, Z. Zhu, S.L. Dvorak, "Exact, closed-form representations for time-domain surface impedances of homogeneous, loosy half-space," *IEEE Trans. Antennas Propag.*, vol. 52, no. 10, pp. 2659–2665, Oct. 2004.

[8] S.L. Dvorak, E.F. Kuester, "Numerical computation of the incomplete Lipschitz-Hankel integral $Je_0(az)$," *Journal of Computational Physics*, vol. 87, no. 2, pp. 301–327, Apr. 1990.

[9] J.G. Maloney, G.S. Smith, "The use of surface impedance concepts in the finite-diference time-domain method," *IEEE Trans. Antennas Propag.*, vol. 40, no. 1, pp. 38–48, Jan. 1992.

[10] S. Kellali, B. Jecko and A. Reineix, "Implementation of a surface impedance formalism at oblique incidence in FDTD method," *IEEE Trans. Electromagn. Compat.*, vol. 35, no. 3, pp. 347–356, Aug. 1993.

[11] B.J. Kooij, "Transient electromagnetic field of a vertical magnetic dipole above a plane plasmonic half-space," *URSI International Symposium on Electromagnetic Theory*, Berlin, Germany, Aug. 2010, pp. 181–184.

Common-Mode Rejection in a Phased-Array Filtenna of Connected Dipoles

Lorenzo Cifola*†, Daniele Cavallo*, Giampiero Gerini*, Silvio Savoia*, Antonio Morini†, Giuseppe Venanzoni†
* TNO, Defence Security and Safety
Oude Waalsdorperweg 63
2597 AK The Hague, Netherlands
{lorenzo.cifola, giampiero.gerini}@tno.nl, d.cavallo@tudelft.nl, silvio.savoia85@gmail.com
† Department of Information Engineering
Università Politecnica delle Marche
via Brecce Bianche, Ancona, Italy
{a.morini, g.venanzoni}@univpm.it

***Abstract*—In this work we describe an effective strategy for the avoidance of common-mode resonances excited in a printed array of loaded dipoles with inherent filtering properties (filtenna). Previous works demonstrated that, for *E*-plane scanning, such resonances occur due to the unbalanced excitation of the dipoles. The present approach is based on the use of an X-band hybrid-ring connected to the filtenna structure. A design with operational bandwidth spanning from 8.5 to 10.5 GHz is presented and validated with simulations.**

I. Introduction

Due to the increasing number of sensors on board of modern military platforms and the growing use of wireless equipment, it is crucial for communication and radar systems to avoid spurious interferences. Therefore, band-pass filters are needed both between the antenna and the Low Noise Amplifiers (LNAs) to avoid receiver desense and in the transmit chain, in order to suppress the emission of harmonic frequency components and to comply with standard regulations for emission outside the operating band. Because of the relatively large physical size of these filters, occupying a large fraction of the available surface when used in phased array applications, new antenna concepts have been recently proposed, where the radiating antenna element itself already performs part or all of the filtering function. Most of these concepts were focused on single antennas or non-scanning arrays [1] - [6].

The design of a new phased array filtenna concept for radar applications was proposed by some of the present authors in [7]. There, a three-pole Tchebychev filter was proposed, which used the radiating element, constituted by capacitively-coupled dipoles in an array configuration, to realize the first pole of the filter. Equivalent circuits for such arrays were developed in [8] and have been exploited for the design. The operational band spans from 8.5 to 10.5 GHz (21% relative bandwidth).

The antenna and the band-pass filter have been integrated in a single module, sufficiently compact to fit within the array unit cell, as shown in Fig. 1. Such an array has been shown to maintain good matching (-10 dB) when scanning in the *H*-plane up to $45\,^{\circ}$. However, for *E*-plane scanning common-mode resonances were observed into the differential lines of the filter due to the unbalanced excitation of the dipoles.

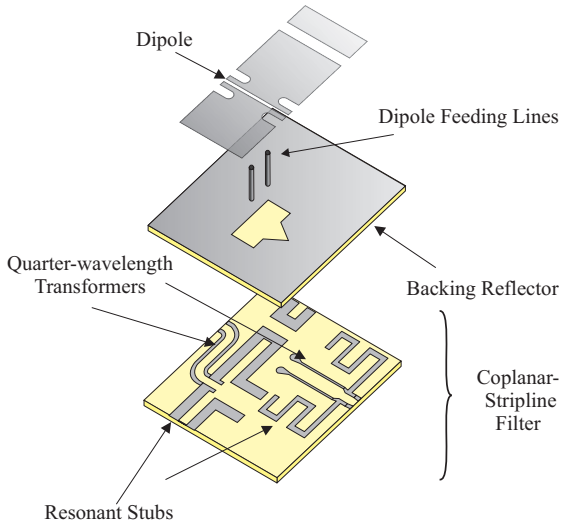

Fig. 1. Exploded view of the array unit cell.

In the present work, a strategy for the common-mode rejection is proposed. It involves the use of an X-band hybrid-ring (*rat-race*), designed with operational bandwidth spanning from 8.5 to 10.5 GHz and connected to the entire structure. The performance is validated by electromagnetic full-wave simulations.

II. Design of an X-band Hybrid-Ring for Common-Mode Rejection

In order to obtain the separation of the signals associated to common-mode and differential-mode, an X-Band hybrid-ring

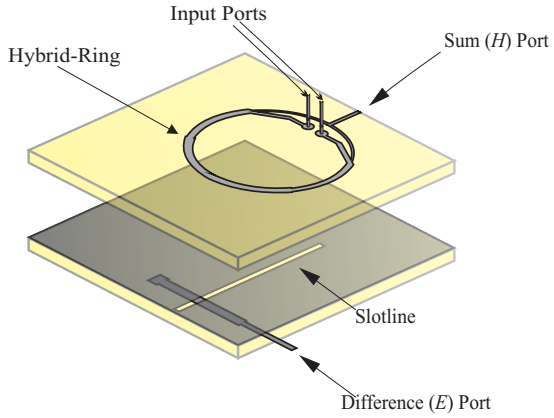

Fig. 2. Exploded view of the X-Band Hybrid-Ring.

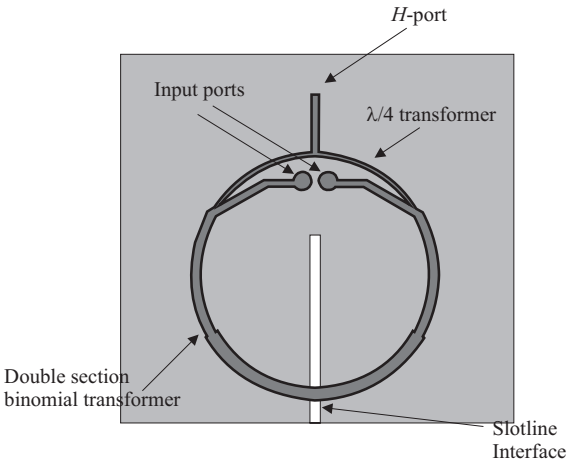

Fig. 3. Top view of the ring circuit.

centered at 9.5 GHz with a bandwidth of about 21% has been designed. As shown in Fig. 2, the device consists of three main elements:

- A ring including the sum (H) port and the input ports;
- A slotline realized in the groundplane used to couple the ring to the difference (E) port by two microstrip-to-slotline transitions;
- A microstrip line realizing the difference port.

Operating as a combiner, the differential-mode signal (desired) is carried at the difference port, while common-mode signal (undesired) is absorbed at the sum port, closed on a matched load.

A. Ring Design

A top-view of the ring circuit is shown in Fig. 3: each of the input ports is connected to the H-port and to the slotline interface by a quarterwave and a double section binomial transformer, respectively.

Considering a odd-mode excitation (corresponding to the desired differential-mode signal), the H-port becomes a virtual ground which is transformed into an open at the input ports. In the case of even-mode excitation (corresponding to the undesired common-mode signal), the E-port is a virtual open transformed into an open at the input ports which are impedance matched with the H-port through a quarter-wavelength transformer [9].

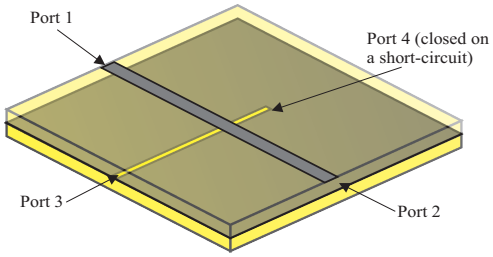

Fig. 4. Hybrid-Ring to Slotline Transition.

B. Slotline Design

The slotline transition consists of two main parts:

- A microstrip to slotline transition used to couple the ring circuit with the slotline;
- A slotline to microstrip transition used to couple the slotline with the E-port.

While the slot length has been tuned by parametric simulation in order to optimize the overall performances of the device, the two transitions have been designed according to an analytical approach that is described in the following sections.

1) Hybrid-Ring to Slotline Transition: starting from a symmetric 4-port network formed by a microstrip-slotline cross junction, we obtain a 3-port network by terminating a slotline branch on a short-circuit, as shown in Fig. 4. The transition is designed in order to obtain perfect matching at port 3.

Given the scattering matrix of the symmetric 4-port network:

$$S = \begin{bmatrix} S_{11} & S_{12} & S_{13} & S_{13} \\ S_{12} & S_{11} & -S_{13} & -S_{13} \\ S_{13} & -S_{13} & S_{33} & S_{34} \\ S_{13} & -S_{13} & S_{34} & S_{33} \end{bmatrix}, \tag{1}$$

the reflection coefficient S'_{33} of the 3-port network obtained by terminating port 4 on a reactive load with reflectivity ρ is defined as:

$$S'_{33} = S_{33} + \frac{S_{34}^2}{\frac{1}{\rho} - S_{33}} \tag{2}$$

Perfect matching condition at port-3 implies:

$$S'_{33} = 0 \tag{3}$$

that, together with (2), becomes:

$$\rho = |\rho|\, e^{j\phi} = \frac{S_{33}}{S_{33}^2 - S_{34}^2} \tag{4}$$

Once forced the reactive load condition ($|\rho| = 1$):

$$|S_{33}| = |S_{33}^2 - S_{34}^2| \tag{5}$$

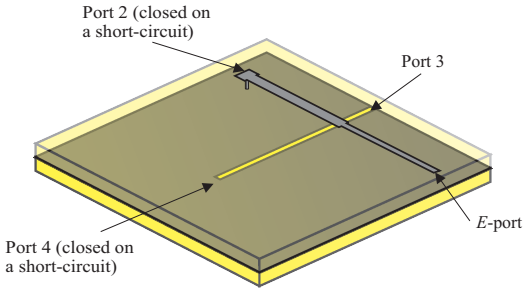

Fig. 5. Slotline to E-port Microstrip Line Transition.

the phase ϕ of the reactive load is obtained solving (4). The distance l from the reference plane of the transition at which the load is placed is then defined as:

$$l = \frac{\pi - \phi}{2\beta} \tag{6}$$

where β is the propagation constant of the line at the midband frequency.

2) Slotline to E-port Microstrip Line Transition: starting from a 4-port network whose scattering matrix is defined by (1), we want to obtain a matched 2-port network by terminating a slotline branch and a stripline arm on short-circuits placed at distance l_1 and l_2 respectively from the reference plane of the junction, as shown in Fig. 5.

The reflection coefficients S'_{11} and S'_{33} of the 3-port network obtained by terminating port 4 on a reactive load of reflectivity ρ_1 are defined as:

$$S'_{11} = S_{11} + \frac{S_{13}^2}{\frac{1}{\rho_1} - S_{33}}, \quad S'_{33} = S_{33} + \frac{S_{34}^2}{\frac{1}{\rho_1} - S_{33}} \tag{7}$$

Terminating port 2 on a short-circuit placed at a distance l_2 from the reference plane of the junction, the resulting 2-port network is matched when [10]:

$$|S'_{11}| = |S'_{33}| \tag{8}$$

for the midband frequency f_0. Such condition is satisfied when:

$$\left(S_{11} + \frac{S_{13}^2}{\frac{1}{\rho_1} - S_{33}} \right) \cdot e^{j\psi} = S_{33} + \frac{S_{34}^2}{\frac{1}{\rho_1} - S_{33}} \tag{9}$$

where ψ is the difference between the phases of S'_{11} and S'_{33}. Solving (9) with respect to ρ_1 we get:

$$\rho_1 = \frac{S_{11}e^{j\psi} - S_{33}}{(S_{11} \cdot S_{33} - S_{13}^2)e^{j\psi} - (S_{33}^2 - S_{34}^2)} \tag{10}$$

Once determined ψ to obtain $|\rho_1| = 1$, it is possible to calculate the position l_1 of the short-circuit in the slot-line with respect to the reference plane of the junction, starting from the phase ϕ of the reactive load:

$$l_1 = \frac{\phi - \pi}{-2\beta} \tag{11}$$

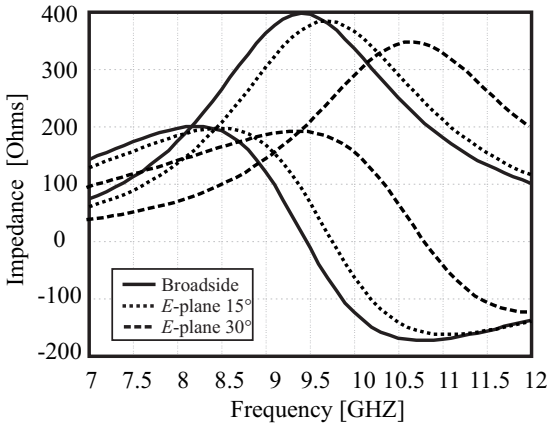

Fig. 6. Active impedance of the dipole when scanning on the *E*-plane

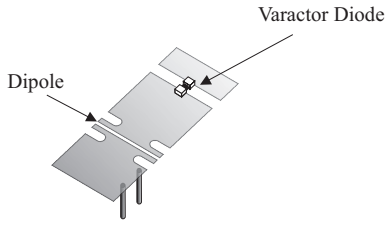

Fig. 7. Varactor diode coupling contiguous dipoles.

At this point, a matched 2-port network is obtained closing port 2 on a short-circuit at a distance l_2 from the reference plane of the junction given by:

$$l_2 = -\frac{1}{2j\beta} \ln \left[\frac{S'_{22}}{\Delta S S'^{*}_{33} \rho_2} \right] \tag{12}$$

where ΔS is the determinant of the 3-port network, β is the propagation constant at the midband frequency and ρ_2 is the reflection coefficient of the reactive load located at distance l_2 from the reference plane of the junction.

C. E-Port

The *E*-port, that could be realized on the same layer of the other ports or on a different layer, is connected to the slotline to microstrip transition.

III. *E*-PLANE SCANNING BEHAVIOUR

Scanning on the *E*-plane produces a shift towards high frequencies of the impedance curve of the dipole, as observed in Fig. 6, causing a substantial detuning of the implemented filter.

In order to overcome this unwanted effect, a varactor diode can be added between contiguous elements, as shown in Fig. 7.

The variable capacitance is used to compensate the dipole resonance frequency shift, avoiding the detuning of the overall filtering structure (Fig. 8).

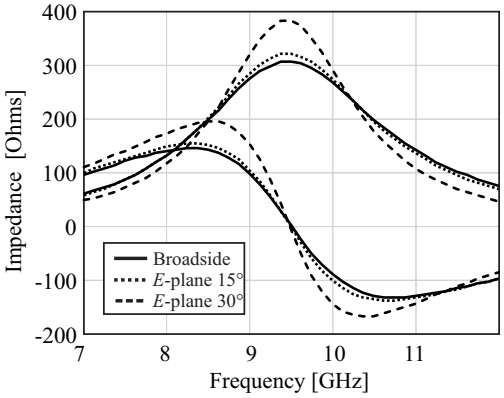

Fig. 8. Active impedance of the dipole tuned by a varactor diode when scanning on the *E*-plane

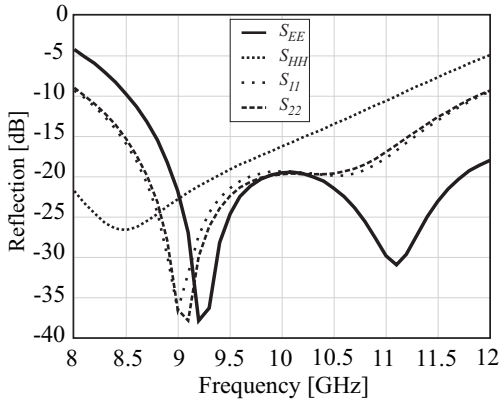

Fig. 9. Reflection performance of the Hybrid-Ring

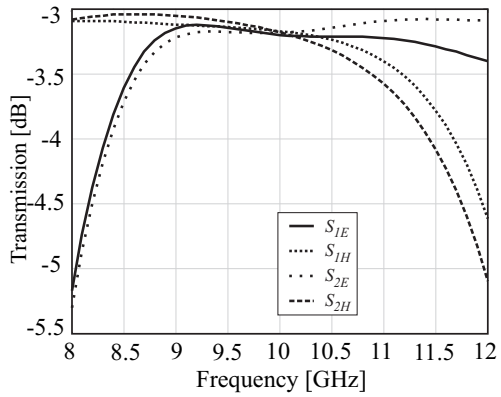

Fig. 10. Transmission performance of the Hybrid-Ring

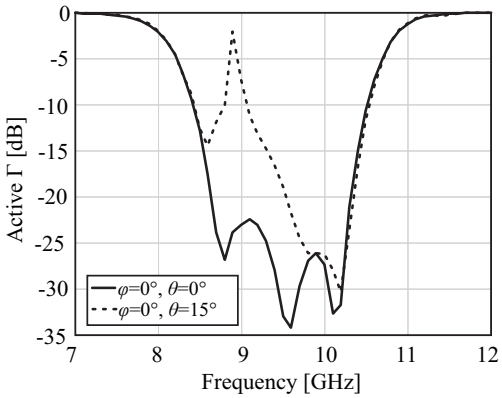

Fig. 11. Filtenna active reflection coefficient for broadside and *E*-plane scan to 15 °.

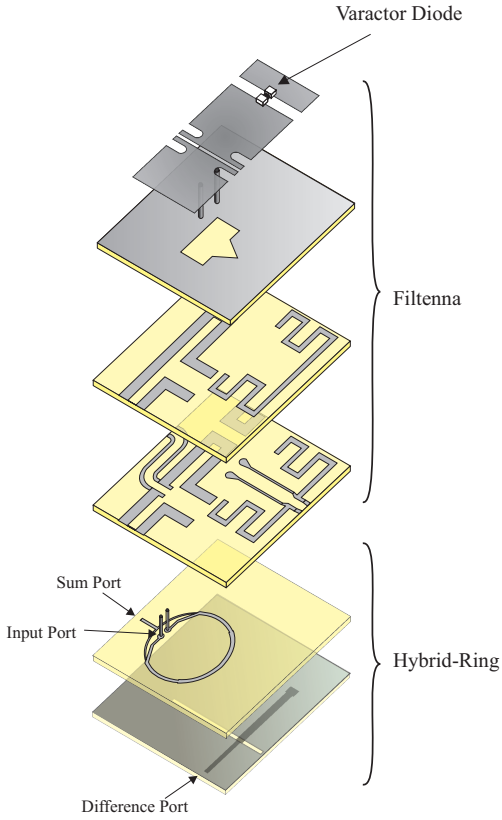

Fig. 12. Exploded view of the array unit cell with the Hybrid-Ring connected to the filtenna structure.

IV. Simulation Results

Reflection and transmission performances of the Hybrid-Ring are shown in Fig. 9 and 10, respectively. Considering the transmission losses of the rat-race (about 0.2 dB) together with that of the filtenna module (about 0.5 dB, [7]), the estimated losses for the entire structure correspond to about 0.7 dB.

The effect of common-mode propagation in the previous filtenna design is highlighted in Fig. 11, which shows the active reflection coefficient for broadside and *E*-plane scan to 15 °: a common-mode resonance is visible at about 8.8 GHz.

The hybrid-ring, as shown in Fig. 12, is connected to the filtenna structure through a bi-wire line.

Electromagnetic simulations of the array unit cell performed by commercial tools assuming periodic boundary conditions, show that the output signal taken at the difference port is resonance-free also for *E*-plane scanning. Indeed, as a result of the combination of the hybrid-ring to the filtenna, the active reflection coefficient does not show any resonance peak, as apparent from Fig. 13.

As regards to the *H*-plane scanning, the structure is capable to reach 45 °, as shown Fig. 14.

A further development, which will be presented at the

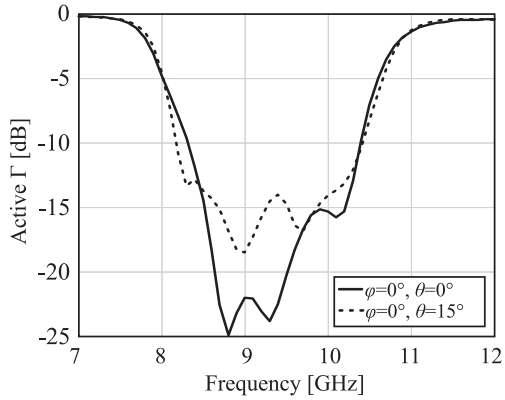

Fig. 13. Active reflection coefficient of the combination of filtenna module and rat-race for broadside and *E*-plane scan to $15\,^\circ$.

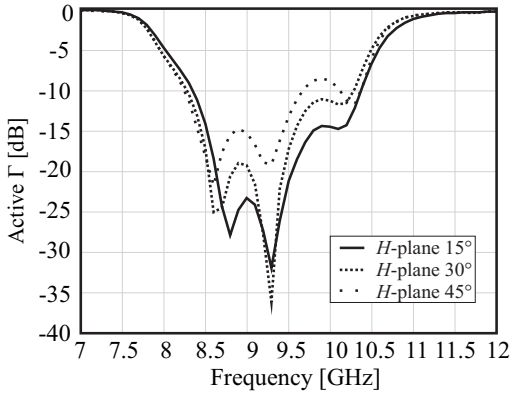

Fig. 14. Active reflection coefficient of the combination of filtenna module and rat-race for *H*-plane scan up to $45\,^\circ$.

conference, consists in the integration of part of the filtering function directly in the hybrid-ring.

V. Conclusions

An effective strategy for the suppression of common-mode resonances in a array of connected dipoles with inherent frequency selectivity properties has been investigated. The common-mode rejection module is based on the use of a planar X-Band Hybrid-Ring connected to the filtenna structure. Furthermore, an analytical approach for the design of microstrip-slotline transitions, used for the coupling between the microstrip ring of the rat-race to the output port, has beeen described. Simulations results show a resonance-free output signal taken at the difference port when scanning on the *E*-plane. Being capable to obtain wide scanning angles mainly on one of the main planes, the present work is addressed to Synthetic Aperture Radar (SAR) applications based on purely planar printed technology. In addition to SAR, other applications requiring scanning only in one plane can be envisaged: these include radar with hybrid mechanical-electronic scanning, where the beam steering is performed electronically in one dimension, while mechanical motion is used for azimuthal scanning.

Acknowledgment

This work has been funded by the FP7-CARE (Coordinating the Antenna Research in Europe) Project.

References

[1] A. Abbaspour-Tamijani, J. Rizk, and G. Rebeiz, *Integration of filters and microstrip antennas,* in Proc. IEEE Antennas and Propag. Int. Symp., San Diego, CA, Aug. 2002, vol. 2, pp. 874-877.

[2] G. Q. Luo, W. Hong, H. J. Tang, J. X. Chen, X. X. Yin, Z. Q. Kuai, and K. Wu, *Filtenna Consisting of Horn Antennas and Substrate Integrated Waveguide Cavity FSS,* IEEE Trans. Antennas Propag., vol. 55, no. 1, pp. 92-98, Jan. 2007.

[3] T. Le Nadan, J. P. Coupez, S. Toutain, and C. Person, *Integration of an antenna/filter device, using a multi-layer, multi-technology process,* in Proc. 28th European Microw. Conf., Amsterdam, Netherlands, Oct. 1998, pp. 672-677.

[4] F. Queudet, I. Pele, B. Froppier, Y. Mahe, and S. Toutain, *Integration of pass-band filters in patch antennas,* in Proc. 32nd European Microw. Conf., Milan, Italy, Sep. 2002, pp. 685-688.

[5] T. Le Nadan, J. P. Coupez, and C. Person, *Optimization and miniaturization of a filter/antenna multi-function module using a composite ceramic-foam substrate,* in IEEE MTT-S Int. Microwave Symp. Digest, Anaheim, CA, Jun. 1999, vol. 1, pp. 219-222.

[6] M. Mandal, Z. N. Chen, and X. Qing, *Compact ultra-wideband filtering antennas on low temperature co-fired ceramic substrate,* in Proc. Asia Pacific Microw. Conf., Singapore, Dec. 2009, pp. 2084-2087.

[7] D. Cavallo, S. Savoia, G. Gerini, A. Neto, and V. Galdi, *Design of a low-profile printed array of loaded dipoles with inherent frequency selectivity properties,* 5th European Conf. Antennas and Propag., Rome, Italy, April 2011, pp. 807-811.

[8] D. Cavallo, A. Neto, and G. Gerini, *Equivalent circuits for connected arrays in transmission and in reception,* IEEE Trans. Antennas and Propag., vol. 59, no. 5, May 2011, pp. 1535-1545.

[9] K. U-yen, E. Wollack, J. Papapolymerou, and J. Laskar, *A Broadband Planar Magic-T using Microstrip-slotline Transitions,* IEEE Trans. Microw. Theory Tech., vol. 56, no. 1, Jan 2008, pp. 172-177.

[10] A. Morini and T. Rozzi, *Constraints to the Optimum Performance and Bandwidth Limitations of Diplexers Employing Symmetric Three-Port Junctions,* IEEE Trans. Microw. Theory Tech., vol. 44, no. 2, Feb 1996, pp. 242-248.

Printed Transition for SIW Horn Antennas - Analytical Model

Marc Esquius Morote, Benjamin Fuchs and Juan R. Mosig
Laboratoire d'Electromagnétisme et d'Acoustique
Ecole Polytechnique Fédérale de Lausanne
Lausanne, Switzerland
marc.esquiusmorote@epfl.ch

***Abstract*—A printed transition is proposed to overcome problems limiting the performances of SIW horn antennas when built in thin substrates (thickness $< \lambda_0/10$). An analytical model to analyze its behavior is given along with design guidelines. The development of a possible transmission line model is also presented.**

This transition is associated with a H-plane sectoral SIW horn antenna to both show the validity of the proposed model and the significant improvements it can bring in terms of matching, bandwidth and radiation.

I. Introduction

The Substrate Integrated Waveguide (SIW) technology allows to construct several types of commonly used antennas in a planar way. However, frequency limitations associated to commercial substrates appear in the implementation of certain types of antennas, e.g., the SIW horns are not well matched when the substrate thickness is much smaller than the wavelength.

One of the main problems of SIW horns is the mismatch between the edge of the dielectric slab and the air which decreases the operational bandwidth. Several strategies have been developed to overcome this problem. Some of them require the use of non-printed elements [1] making the building procedure more complicated. Solutions based on integrated dielectric lenses [2], [3] have also been proposed but their performances are limited by the thickness of the substrate.

In this paper, a printed transition to improve the matching between thin substrate SIW horn antennas and the air is proposed. The transition is etched on the same dielectric slab as the antenna and does not require the use of non-printed elements. This eases the manufacturing process while keeping the advantages of both compactness and integration of the SIW technology. A sectoral H-plane SIW horn with the proposed transition is represented in Fig. 1.

II. Analytical Model

Let us consider a dielectric parallel plates, i.e., a dielectric slab metalized in both sides. Slots are etched on each side of the metallic plates as represented in Fig. 2. This structure is infinite along the width (z direction) defining a 2D problem with the variables: length of the metallic strip *L*, slot size *s*, substrate thickness *h* and relative permittivity ε_r.

This structure can be seen as a concatenation of blocks, each one being a parallel plate waveguide separated by a distance

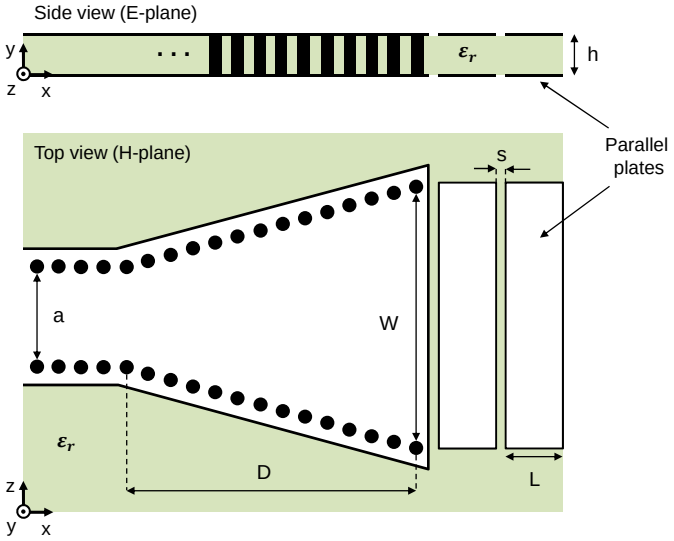

Fig. 1. Side and top view of a SIW horn with the proposed printed transition to the air.

s. The resonant frequency fr_0 of one block is approximated by the use of an equivalent length L_{eq}, where $L_{eq} > L$ due to the effect of the fringing fields. This effect depends on both *h* and *L* and, under the conditions established in [4], fr_0 is given by:

$$fr_0 = \frac{c}{2L_{eq}\sqrt{\varepsilon_r}} = \frac{c}{2L(1+0.7h/L)\sqrt{\varepsilon_r}}. \qquad (1)$$

A. Two block structure

When two blocks are separated a distance *s*, charges build up on the ends of the metallic plates describing a capacitance which produces a shift in the resonant frequency fr_0. The value of this capacitance per unit of length, C_S, can be

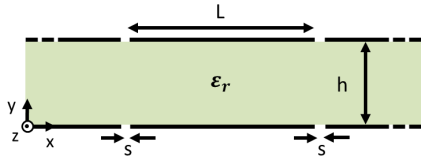

Fig. 2. Cutting view of the structure with the associated notations

obtained using the conformal mapping technique [5]. Thus, considering that $s/h << 1$, C_S is given as follows:

$$C_S = \varepsilon_0(\varepsilon_r + 1)\frac{K(k')}{K(k)} \tag{2}$$

with

$$k = \sqrt{\frac{1 + L_1/s + L_2/s}{(1 + L_1/s)(1 + L_2/s)}} \tag{3}$$

where $K(k)$ is the complete elliptic integral of the first kind and $k' = \sqrt{1 - k^2}$. The lengths of the metallic plates at each side of the slot are noted as L_1 and L_2. In the current case, to equal blocks are concatenated meaning that $L_1 = L_2 = L$.

In the theory of coupling resonators, a coupling factor is used to calculate the shift in fr_0. This factor is defined as the quotient between the capacitance generated by the coupling effect, C_C, and the capacitance of the original structure, C_0. In the case of two blocks, C_C is $C_S/2$ because the slots in the top and bottom faces are in series and C_0 is twice the capacitance between the two metallic parallel plates of one block, $2C_P$.

When computing C_P, the effect of the fringing fields must be considered. This effect is only relevant at the exterior faces while at the junction between blocks can be neglected. Following the approach presented in [6], the capacitance per unit of length of C_P can be estimated by:

$$C_P \simeq \frac{\varepsilon_0\varepsilon_r L}{h}\left(1 + \frac{h}{\pi L} ln\left(\frac{\pi L}{h}\right)\right). \tag{4}$$

The physical explanation of this frequency shift is that the coupling effect reduces the capability to store charge of a single block [7]. Therefore, the coupling factor has a negative value and frequencies higher than fr_0 are obtained:

$$fr_1 = \frac{fr_0}{\sqrt{1 - C_C/C_0}} \tag{5}$$

Following the similitude with coupled microstrip resonators, the coupling effect also enhances the storage capability obtaining lower frequencies. However, the lack of ground plane in the presented structure diminishes this enhancement obtaining slightly different frequencies from the ones expected using the microstrip theory.

B. N block structure

For a proper use of this model, several aspects should be taken into account when more blocks are concatenated. As an example, a structure of 3 blocks is now considered. An sketch of the electric field in the upper part of this structure is presented in Fig. 3.

Since the central metallic plate contributes to generate two capacitances, the new value for each C_S is calculated with (2) using $L_1 = L$ and $L_2 = L/2$. This approximated capacitance is valid for $s/L << 1$ and provides a physical insight on the behavior of this structure without the need to apply conformal mapping for each scenario. In addition, now the middle block has no exterior faces which means that its C_P is computed neglecting the fringing fields effect. Therefore, its per unit length value is $\varepsilon_0\varepsilon_r L/h$.

TABLE I
RESONANT FREQUENCIES FOR DIFFERENT NUMBER OF BLOCKS
(L = 3MM, h = 1.25MM, s = 0.12MM, $\varepsilon_r = 3.27$)

Number of Blocks	**Full-wave simulation** (GHz)	**Analytical Model** (GHz)
1	21.62	21.40
2	18.42	19.15
	23.45	23.65
3	17.31	18.24
	20.52	21.40
	24.50	24.56

To validate the proposed approach, the resonant frequencies of 1 to 3 block structures are computed using full-wave simulations and compared with the ones obtained using the presented analytical model. Table I shows that the resonances above fr_0 are predicted with high accuracy (relative error $< 2\%$) while, as expected, a higher error appears concerning the ones below ($\sim 6\%$).

This analytical model allows for a quick prediction of the resonant frequencies of this kind of structures. However, when quantitative information about the return loss is required, more aspects need to be considered: source and load impedances, propagating modes, radiation losses, etc. Therefore, a Transmission Line model is proposed in section III.

III. TRANSMISSION LINE MODEL

A Transmission Line (TL) model is proposed to analyze the behavior of the printed transition. The transition is also decomposed into blocks but this time the width *W* in the z direction is taken into account defining a 3D problem. Referring to Fig. 1, each block is formed by a slot (modeled as a capacitance C_S in parallel with a radiation resistance R_{rad}) and a parallel plate waveguide (defined by its characteristic impedance and propagation velocity). The values of the different C_S are obtained using the expressions presented in section II and the R_{rad} can be seen as the one of an uniform distribution aperture [8]. The open-ended termination of the last parallel plate waveguide is modeled by an impedance given in [9].

In the studied scenario, a transition created by several blocks is placed in front of an antenna in order to smooth its transition

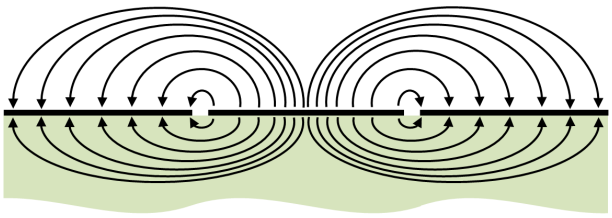

Fig. 3. Electric field in the half upper part of a 3 blocks structure

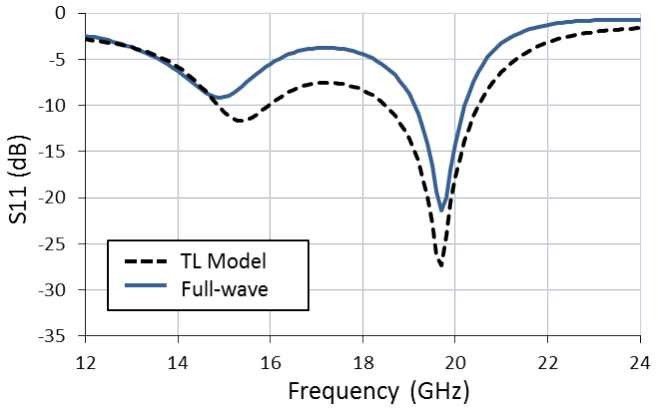

Fig. 4. Return loss of a 2 block transition. Comparison between full-wave simulations and the TL model

to the air. As an example, a 2 block transition is placed in front of a SIW with the following parameters [mm]: $L = 3.8$, $s = 0.15$, $W = 7$. A commercial substrate Rogers RT/duroid 6002 ($\varepsilon_r = 2.94$) with a thickness h = 1.524 mm is used. Fig. 4 presents the return loss comparison between the TL model and full wave simulations. The TL model provides a good approximation concerning the position and shape of the resonances.

In this scenario, fr_0 is 17.9GHz. As mention in II-A, the resonance at 14.8GHz is due to the enhancement in the storage capability obtained with the coupling effect. In general, these resonances below fr_0 present a poor matching ($S11 >$ -10dB) being of less interest than the ones above fr_0. More accurate explanations and details of this TL model will be presented in a forthcoming paper.

IV. Design Guidelines

Applying the analytical model described in section II, it is possible to design a transition working at any desired frequency. However, the following trends should be kept in mind when it comes to choose the values of *L*, *s*, *h* and ε_r: an increase in the ratio *h/L* improves the matching and bandwidth but other modes might be excited; reducing the ratio *s/L*, diminishes the radiation losses, but also the slot transition becomes more abrupt losing bandwidth. Furthermore, in order to guarantee a proper behavior of SIW structures for end-fire radiation, ε_r should present a low value. A reasonable trade-off is the following: $0.25 < h/L < 0.5$, $0.03 < s/L < 0.06$, $\varepsilon_r < 5$. Note that the accuracy of the proposed model will decrease when reaching the limits of these boundaries.

To design the transition as a transformer between the antenna and the air impedance, a recommended starting point is to set to $L = 0.4\lambda_0/\sqrt{\varepsilon_r}$. Afterwards, in order to define the different resonances, initial values for *h* and *s* are obtained with (1)-(5) while respecting the range of values previously defined. Finally, the TL model allows to further tune the dimensions of the transition before doing a final verification with full-wave simulations.

V. Application with a SIW Horn Antenna

Let us consider that a H-plane sectoral SIW horn antenna working around 17GHz wants to be designed in a Rogers RO3203 substrate ($\varepsilon_r = 3.02$, h = 1.52mm). As stated in the introduction, at this frequency range, a SIW horn has a poor performance in terms of return loss due to its small thickness ($\sim \lambda_0/11$). In order to improve the return loss of the horn, the proposed transition to the air is used.

The dimensions of the SIW horn (*a*, *D* and *W* in Fig. 1) are chosen according to the design rules given in [10]. In order to eliminate the higher order modes in the waveguide, to guarantee a single mode at the horn aperture and to obtain acceptable quadratic phase error, the parameters have been chosen as follows [mm]: $a = 9$, $W = 20$, $D = 19$.

The width of the transition is determined by the width *W* of the horn aperture. The electric field distribution outside the horn, i.e., at the beginning of the transition, can be approximated as the one of an equivalent waveguide of width *W* where only the TE_{10} mode is considered.

The single SIW horn antenna has, as expected, a poor matching (see Fig. 5(a)). The procedure described in IV is followed to obtain a working frequency band ($S11 < -10dB$) at 16.5GHz with a 1 block transition, and two others at 15.5 and 18.5Hz with a 3 block transition. The values found are $L = 4.2$mm and $s = 0.17$mm.

A 7% bandwidth is obtained with a printed transition of only 1 block (see Fig. 5(b)). Using a 3 block transition, two other bands of 4.5% and 2.5% bandwidth are achieved (see Fig. 5(c)). As explained in section III, the lowest resonance generated using 3 blocks presents a poor matching and is not useful under the established conditions. The results also show the good agreement between the analytical model, the TL model and full-wave simulations.

VI. Further Improvements

Another critical aspect of the standard SIW horn antenna is the low front-to-back ratio (FTBR) which is smaller than 3dB. This considerably reduces the directivity which is an important drawback in a lot of applications.

The transition described in the previous sections, does not significantly modifies the radiation characteristics of the standard SIW horn. Nevertheless, few modifications can be introduced to partially cancel the unwanted back radiation due to refraction effects, e.g., designing a periodicity along the transition width. In Fig. 6, an example of a 12dB FTBR improvement using a triangular periodicity is presented. Further details and examples will be provided in a forthcoming paper.

VII. Conclusions

A printed transition to overcome problems limiting the performances of SIW horn antennas has been proposed. Analytical and transmission line models to analyze the behavior of the transition have been also presented. They allow for a quick prediction of its resonance frequencies as well as accurate preliminary results for the return loss. Design guidelines

and recommendations concerning the effect of the transition dimensions are given.

This transition is associated with a H-plane sectoral SIW horn antenna built in a thin commercial substrate ($\sim \lambda_0/11$) to show both the validity of the proposed models and the significant improvements it can bring in terms of matching and bandwidth. Modifications in this transition in order to improve the radiation characteristics are commented.

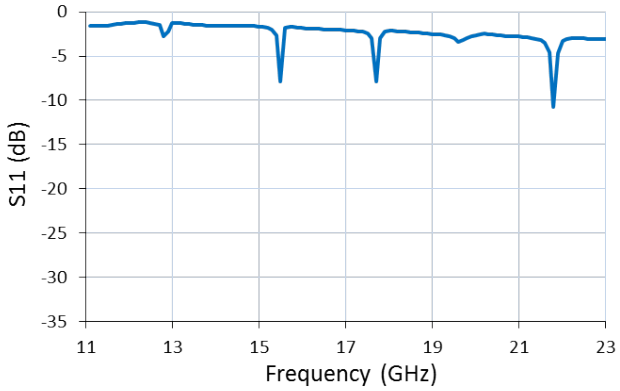

(a) No transition

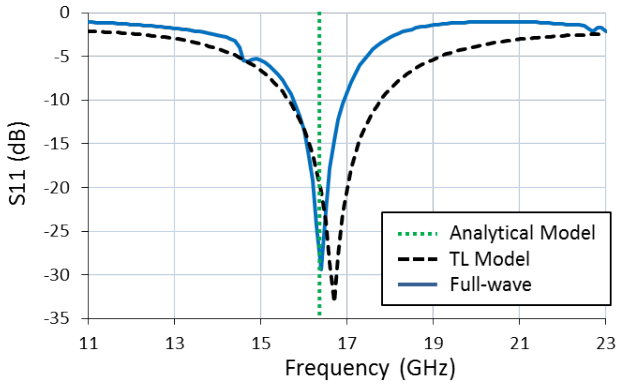

(b) 1 block transition

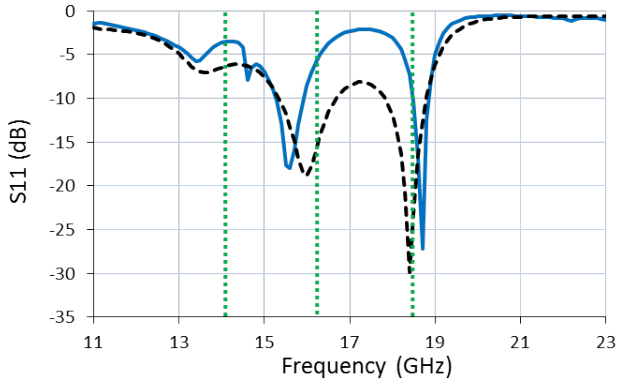

(c) 3 block transition

Fig. 5. Return loss of the SIW horn antenna with different transitions. Comparison between full-wave simulations and the analytical and TL models

Applying the proposed transition, the lower frequency limit for the use of SIW horn antennas (associated to the thickness of commercial substrates) can be extended making them attractive for many other applications.

ACKNOWLEDGMENTS

M. Esquius Morote was supported during his 3-months stay at EPFL Switzerland by the Coordinating the Antenna Research in Europe (CARE) Project, an EU-FP7 Funded Coordination.

REFERENCES

[1] Z. Li, X.-P. Chen, and K. Wu, "A surface mountable pyramidal horn antenna and transition to substrate integrated waveguide," in *International Symposium on Signals, Systems and Electronics*, Aug. 2007, pp. 607 –610.

[2] W. Che, B. Fu, P. Yao, and Y. L. Chow, "Substrate integrated waveguide horn antenna with dielectric lens," *Microwave and Optical Technology Letters*, vol. 49, pp. 168 –170, 2007.

[3] H. Wang, D.-G. Fang, B. Zhang, and W.-Q. Che, "Dielectric loaded substrate integrated waveguide (siw) h-plane horn antennas," *IEEE Transactions on Antennas and Propagation*, vol. 58, no. 3, pp. 640 –647, march 2010.

[4] K. Yazdandoost and D. Gharpure, "Simple formula for calculation of the resonant frequency of a rectangular microstrip antenna," in *IEEE 5th International Symposium on Spread Spectrum Techniques and Applications*, vol. 2, Sep. 1998, pp. 604 –605 vol.2.

[5] S. Bedair, "Characteristics of some asymmetrical coupled transmission lines (short paper)," *IEEE Transactions on Microwave Theory and Techniques*, vol. 32, no. 1, pp. 108 – 110, Jan. 1984.

[6] M. H. Bao, *Handbook of sensors and actuators*, 2000, vol. 8, p. 144.

[7] J.-S. Hong and M. Lancaster, *Microstrip filters for RF/microwave applications*. Wiley, 2001, ch. 8.2.

[8] C. A. Balanis, *Antenna Theory Analysis and Design*. Wiley, 2005, ch. 12.5.

[9] J. James and P. Hall, *Handbook of microstrip antenna 1*. IEE, 1989, ch. 10.2.

[10] D. Deslandes and K. Wu, "Accurate modeling, wave mechanisms, and design considerations of a substrate integrated waveguide," *IEEE Transactions on Microwave Theory and Techniques*, vol. 54, no. 6, pp. 2516 –2526, june 2006.

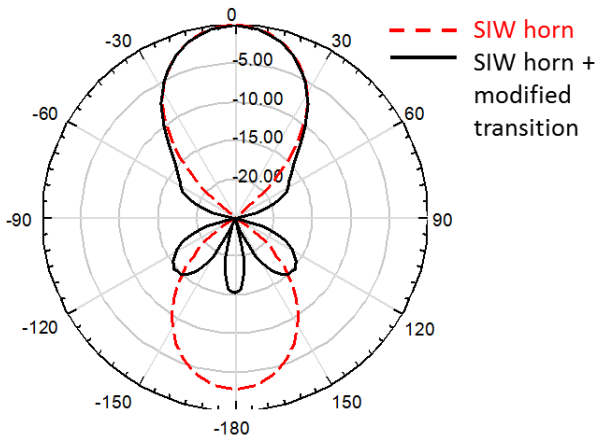

Fig. 6. Normalized directivity of the standard SIW horn and with the modified transition at 13 GHz (H plane)

A MATLAB-based Virtual Tool for Visualizing the Plane Wave Propagation in Multilayer Structures Containing Metamaterials

Marcin Wielichowski* and Juan R. Mosig†
*Faculty of Microsystem Electronics and Photonics (WEMiF)
Wrocław University of Technology
Wrocław, Poland
marcin.wielichowski@pwr.wroc.pl
†Laboratory of Electromagnetics and Acoustics (LEMA)
Ecole Polytechnique Fédérale de Lausanne (EPFL)
ELB-Station 11, CH-1015 Lausanne, Switzerland
juan.mosig@epfl.ch

Abstract—**The paper reports on a graphical user interface developed in MATLAB to aid the visualization of the plane wave impinging from a lossless half-space onto a multilayer structure. Individual layers are assumed to be homogeneous and isotropic with electric permittivity (ε) and magnetic permeability (μ) taking arbitrary complex values. Double-positive, single-negative and double-negative media (real parts of ε and μ) as well as lossless, dissipative and amplifying media (imaginary parts of ε and μ) are allowed. 2D field distribution, transmission and reflection coefficients, and the wave vectors' *z*-component locations in the complex plane are presented to the user.**

Keywords-electrical engineering education; graphical user interfaces; electromagnetic propagation; electromagnetic refraction; nonhomogeneous media

I. INTRODUCTION

By utilizing the MATLAB's graphical and interactive capabilities, the understanding of wave propagation phenomena can be aided. The graphical user interface (GUI) presented in the paper is focused on visualizing the plane wave interaction with multilayer structures and a proper (physical) sign of square root selection for the wave vector value when no limitations are imposed on the values of complex ε and μ. In particular, observation of negatively refracted propagating waves in double-negative materials (metamaterials) is possible.

II. ANALYSIS

The structure under consideration is depicted in Fig. 1. It consists of n layers (regions 2 through n-1) and two semi-infinite spaces (regions 1 and n). We follow [1] in the analysis of plane wave propagation inside the structure. In what follows, we use ε and μ for the relative electric permittivity and relative magnetic permeability, respectively.

In the TE case, imposing the continuity of E_x and H_y at each boundary, we arrive at the following equations for the amplitudes, E_l^+ and E_l^-, of E_x in the neighboring regions l and l+1:

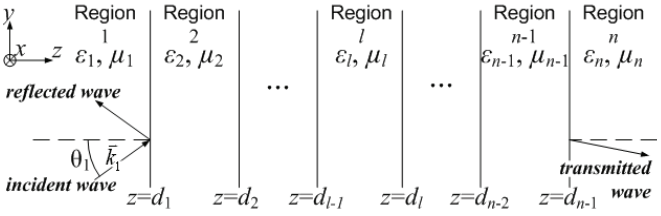

Figure 1. The multilayer structure.

$$E_l^+ e^{ik_{lz}d_l} + E_l^- e^{-ik_{lz}d_l} = E_{l+1}^+ e^{ik_{(l+1)z}d_l} + E_{l+1}^- e^{-ik_{(l+1)z}d_l}, \quad (1)$$

$$E_l^+ e^{ik_{lz}d_l} - E_l^- e^{-ik_{lz}d_l} = p_{l(l+1)}\left[E_{l+1}^+ e^{ik_{(l+1)z}d_l} + E_{l+1}^- e^{-ik_{(l+1)z}d_l}\right], \quad (2)$$

where the superscripts "+" and "–" denote waves propagating towards the increasing or decreasing values of the z-coordinate, respectively, and

$$\text{TE:} \quad p_{l(l+1)} = \frac{\mu_l k_{(l+1)z}}{\mu_{l+1} k_{lz}}, \quad \text{TM:} \quad p_{l(l+1)} = \frac{\varepsilon_l k_{(l+1)z}}{\varepsilon_{l+1} k_{lz}}. \quad (3)$$

Equations (1) and (2) remain valid for the TM case after applying the substitution: $E_x \rightarrow H_x$. In (3), k_{lz} denote the z-direction component of the wave vector in individual regions.

Within a given region, from the dispersion relation for isotropic medium

$$\left|\bar{k}_l\right|^2 = k_y^2 + k_{lz}^2 = \varepsilon_l \mu_l, \quad (4)$$

k_{lz} is found to be

$$k_{lz} = \pm\sqrt{\varepsilon_l \mu_l - k_y^2}\,. \quad (5)$$

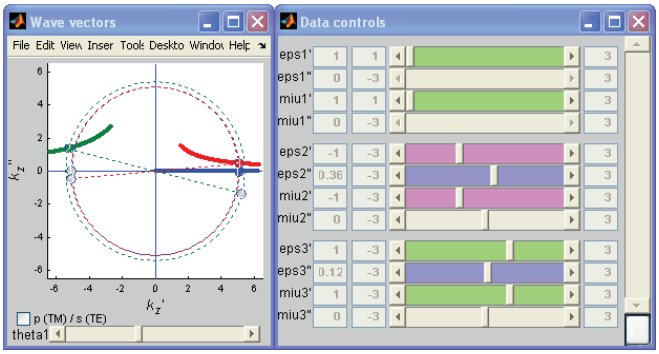

Figure 2. The "Data Controls" and "Wave Vectors" windows.

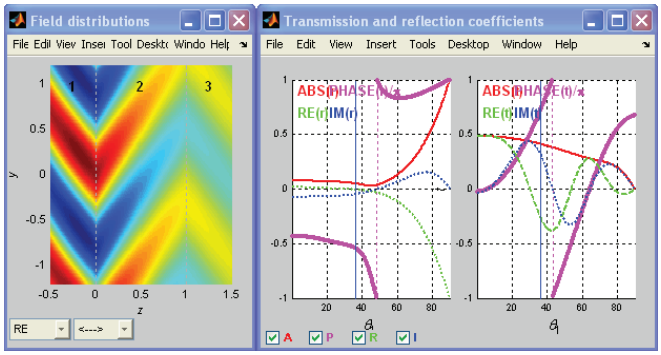

Figure 3. The "Field Distribution" and "Transmission and Reflection Coefficients" windows.

Value of k_y is preserved across the multilayer structure due to the phase matching condition at the boundaries.

In individual regions, the physically correct sign of the square root in (5) is selected according to the procedure described in [2-4]. The procedure defines a mapping between the k_z^2 and k_z complex planes by placing the square root's branch cut along the negative imaginary axis. For non-propagating (evanescent) waves, attenuation is imposed in all types of media.

Transfer matrix technique is employed in solving the system of equations resulting from (1) and (2) applied to each layer boundary in the structure. Thus, wave amplitudes E_l^+ and E_l^- as well as reflection and transmission coefficients are found.

III. Description of the GUI

The main design goals for the GUI were:

- an easy access to a set of predefined multilayer structures demonstrating various aspects of plane wave propagation, and
- a possibility of interactively adjusting the wave polarization, the angle of wave incidence and all geometrical (layer thickness) and material (real and imaginary parts of ε and μ) parameters of the structure.

A set of (human-readable) XML files has been created. The files contain definitions of multilayer structures intended to demonstrate the physical phenomena like: wave attenuation, wave amplification, evanescent waves, negative refraction, excitation of guided modes, or excitation of surface plasmons. Files can be imported into the GUI.

The GUI comprises four separate, resizable windows: "Data Controls", "Wave Vectors", "Field Distribution", and "Transmission and Reflection Coefficients", as shown in Fig. 2 and Fig. 3. The adjusting of individual parameters is realized by means of the standard GUI elements (controls). Individual windows are briefly described below.

A. *"Data Controls"*

A set of sliders is assigned to each region of the structure. The sliders enable the adjusting of region thickness and (see Fig. 2) material parameters ε and μ of the region. Both real and imaginary parts of ε and μ are accessible.

B. *"Wave Vectors"*

A slider and a check-box are available for adjusting the angle of incidence and the polarization of the plane wave, respectively.

The user is presented with a plot representing the k_z complex plane (see Fig. 2). Locations of k_z values in individual regions are marked with numbered circles. To see the consequences of a physically incorrect selection of k_z, the user is free to select alternative values of k_z by using the mouse click. Paths on the complex plane along which k_z values "travel" as the incidence angle changes between 0° and 90°, are plotted as thick solid lines.

C. *"Field Distribution"*

A 2D plot of the field component E_x or H_x, depending on the polarization selected, is available (see Fig. 3). Layer boundaries are marked with dashed lines. By using the dedicated drop-down menus, the user can change the type of the plot (real part, absolute value, or phase) and the propagation direction of waves being shown in the plot (reflected and transmitted, only reflected, or only transmitted waves).

D. *"Transmission and Reflection Coefficients"*

Two separate plots show the reflection and transmission coefficients in a function of the incidence angle (see Fig. 3). By using the dedicated check-boxes, the user can select the data being displayed (absolute value, phase, real part, or imaginary part of the coefficients).

IV. Example Structures

Below, there are presented several example multilayer structures together with screenshots of selected GUI windows. The examples presented are intended to illustrate the educational value of the software.

A. *TE Brewster Angle and Total Internal Reflection*

Setting up a structure consisting of two half-spaces of the

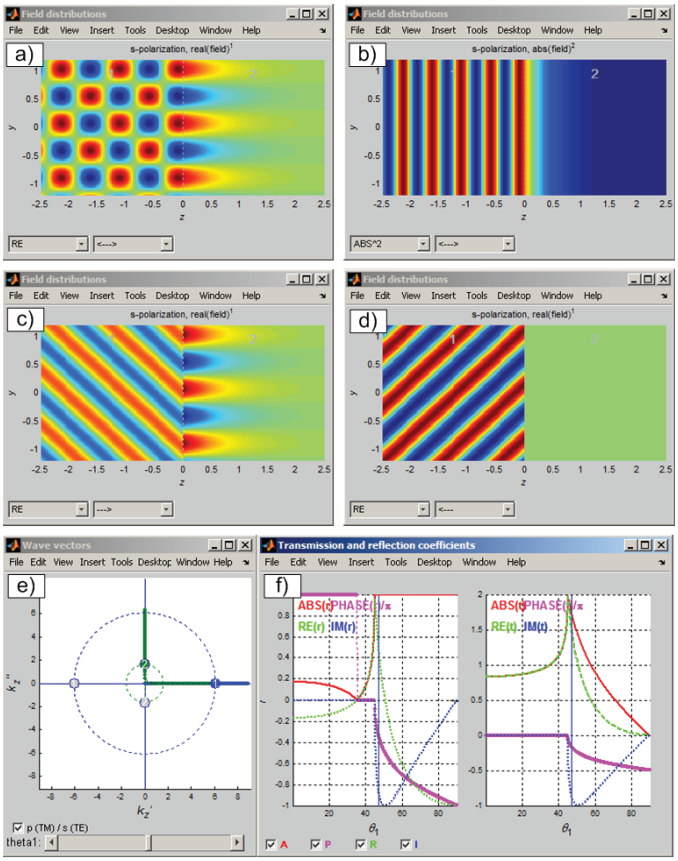

Figure 4. The TE-polariation Brewster angle and the total internal reflection in a two-media structure composed of double-positive materials. (See decription in text).

following parameters: $\varepsilon_1 = 1$, $\mu_1 = 2$ and $\varepsilon_2 = \mu_2 = 1$, allows to interactively study the Brewster angle and the total internal reflection (TIR) phenomena. Since magnetic permeabilities of both media are different, unlike the case of most conventional materials in which electric permittivities differ, the Brewster angle exists for the TE-polarized waves, not for the TM waves.

Figure 4. shows some instructive views produced with the GUI. Diagrams a,b) and c,d) have been created by manually modifying the following parameters available to the user: the electric field component (real part or absolute value squared) and direction of wave propagation (towards increasing or decreasing values of z). The thick green line in diagram e) marks the k_{2z} loci in function of the incidence angle. It is evident that TIR is being realized because the current value of k_{2z} is purely imaginary (see the green circle's position). Incidence angle values corresponding to the Brewster angle and TIR, can easily be estimated from the diagram f). They correspond to zero and (the onset of) unity values of the reflection coefficient, respectively.

B. *ε-negative and μ-negative Materials*

A brief comparison of ε-negative (ENM) and μ-negative (MNM) materials can be performed by defining two structures, each one consisting of two half-spaces, characterized by: $\varepsilon_1 = \mu_1 = \mu_2 = 1$, $\varepsilon_2 = -3$, and $\varepsilon_1 = \mu_1 = \varepsilon_2 = 1$, $\mu_2 = -3$. TE polarization is considered.

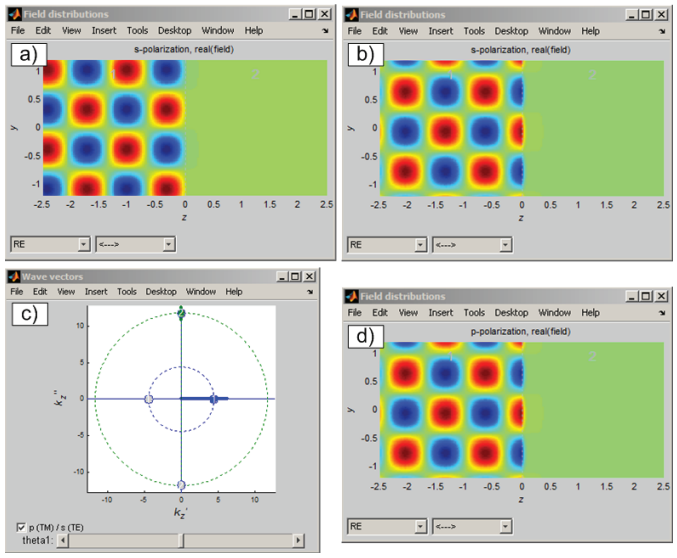

Figure 5. Comparison between ENM and MNM materials. (See decription in text).

One can observe in Fig. 5, the media boundary being located close to the electric field minimum in the metal-type, ENM case shown in diagram a). In the magnetic conductor-type, MNM case shown in diagram b), the media boundary lays close to the electric field maximum. This latter situation is in analogy with the metal-like case, but with the magnetic field being displayed and polarization changed from TE to TM (diagram d)). In all cases discussed, k_z loci are identical and are visible in diagram c). In particular, k_{2z} is always purely imaginary thus both ENM and MNM media do not support propagating waves.

C. *Guided Waves*

To demonstrate the idea of guided modes in planar structures, the method of evanescent coupling is employed. Refractive index values in media 1. and 3. are defined to be higher than those in media 2. and 4. For incidence angles above the TIR angle, electromagnetic energy can be coupled from medium 1. to 3. by means of evanescent wave excited in medium 2. Numerical values being applied are: $\varepsilon_1 = \varepsilon_3 = 1.5$, with all other parameters equal 1.

Several situations are depicted in Fig. 6. Before the TIR angle is reached, a significant amount of electromagnetic energy is transmitted through the multilayer structure (diagram a)). For higher incidence angles, above the TIR angle, there are two possibilities: either waves are reflected (diagram c)) much like in the simple two-media case (compare Figure 4.; however, now this is the so called frustrated TIR due to some amount of energy existing as propagating wave in medium 4.), or one of the guided modes is excited (diagrams b) and d)). The structure under consideration supports three guided modes which is manifested as three maxima of the transmission coefficient visible the in the diagram e).

D. *Surface Plasmon with Gain*

A somewhat less typical multilayer structure proposed in

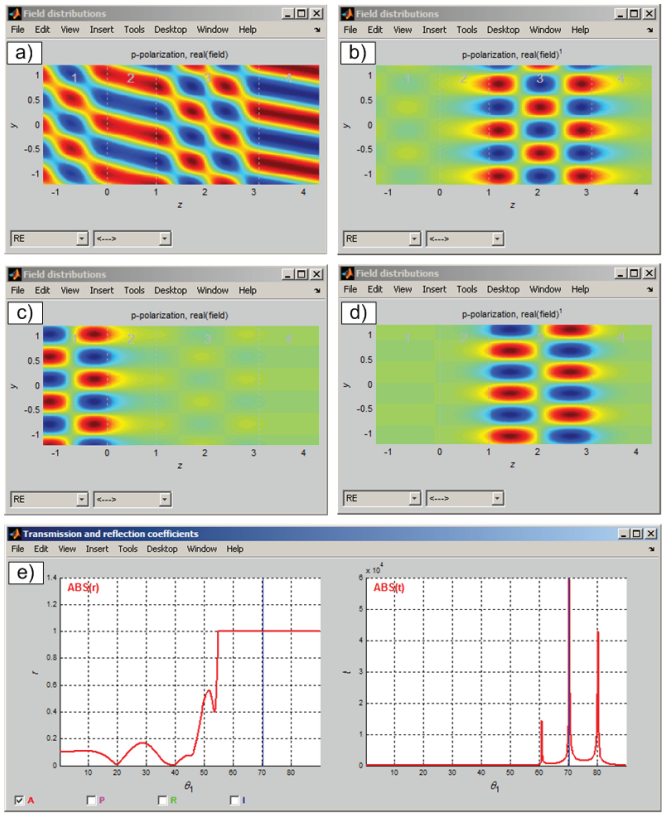

Figure 6. Guided mode excitation by means of evanescent coupling. (See decription in text).

[4], will be considered. Medium 2., a metallic layer, is adjacent to a semi-infinite space, medium 3., that shows amplification. A plane wave incident from medium 1. can excite a surface plasmon at the boundary between 2. and 3. (Surface plasmon propagation is also supported when medium 3. is either lossless or lossy).

Both magnetic field and electromagnetic energy distributions are shown in diagram a), Fig. 7. Values of k_{2z} and k_{3z} are located close to the imaginary axis (green and red circles in diagram b)). This is due to the evanescent nature of surface plasmons on both sides of media boundary. A sharp decrease in the reflection coefficient visible in diagram c), marks the angle at which the surface plasmon is excited.

V. SUMMARY

The educational software tool, a GUI developed in Matlab, presented in this paper, provides a straightforward way to construct multilayer structures of arbitrary material parameter

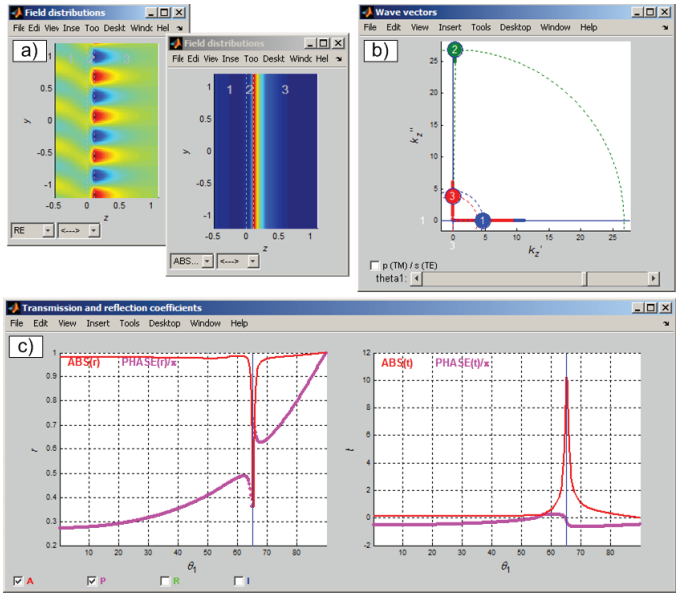

Figure 7. Surface plasmon excited along boundary between a metallic and a double-positive amplifying media. (See decription in text).

values and to visualize the plane wave interaction with the structures.

Though the software has not been used in student lab so far, it seems that, thanks to the visual approach combined with strong interactive capabilities, full understanding as well as memorizing of a number of details connected with plane wave propagation, can be significantly enhanced. Gaining some physical intuitions not immediately obvious from formal derivations, is also made more accessible.

M. Wielichowski was supported during his 6-months stay at EPFL Switzerland by the Coordinating the Antenna Research in Europe (CARE) Project, an EU-FP7 Funded Coordination Action.

REFERENCES

[1] J. A. Kong, "Electromagnetic wave interaction with stratified negative isotropic media," Progress In Electromagnetics Research, vol. 35, pp. 1–52, 2002.

[2] S. A. Ramakrishna and O. J. Martin, "Resolving the wave vector in negative refractive index media," Opt. Lett., vol. 30, pp. 2626–2628, 2005.

[3] A. A. Govyadinov, V. A. Podolskiy, and M. A. Noginov, "Active metamaterials: Sign of refractive index and gain-assisted dispersion management," Appl. Phys. Lett., vol. 91, pp. 191103, 2007.

[4] M. A. Noginov, V. A. Podolskiy, G. Zhu, M. Mayy, M. Bahoura, J. A. Adegoke, B. A. Ritzo, and K. Reynolds,"Compensation of loss in propagating surface plasmon polariton by gain in adjacent dielectric medium," Opt. Express, vol. 16, pp. 1385–1392, 2008.

The CARE Final Workshop has been organized joined with the EuCAP2012 Conference, in Prague. This excellent dissemination result has been achieved, further to the **CARE support**, thanks to the excellent relations between the **CARE project** and the European Association on Antenna and Propagation (EurAAP), owner of the EuCAP Conference.

The CARE consortium believes that the **CARE Final Workshop** represents a valuable event for the spreading of the **CARE results**, especially towards the New Member States.